

## Statistical Properties of the Population of the Galactic Center Filaments II: The Spacing Between Filaments

F. YUSEF-ZADEH,<sup>1</sup> R. G. ARENDT,<sup>2,3</sup> M. WARDLE,<sup>4</sup> S. BOLDYREV,<sup>5</sup> I. HEYWOOD,<sup>6,7</sup> W. COTTON,<sup>8</sup> AND F. CAMILO<sup>9</sup>

<sup>1</sup>*Dept Physics and Astronomy, CIERA, Northwestern University, 2145 Sheridan Road, Evanston, IL 60207, USA  
(zadeh@northwestern.edu)*

<sup>2</sup>*Code 665, NASA/GSFC, 8800 Greenbelt Road, Greenbelt, MD 20771, USA*

<sup>3</sup>*UMBC/CRESST 2 (Richard.G.Arendt@nasa.gov)*

<sup>4</sup>*School of Mathematical and Physical Sciences, Research Centre for Astronomy, Astrophysics and Astrophotonics, Macquarie University, Sydney NSW 2109, Australia, (mark.wardle@mq.edu.au)*

<sup>5</sup>*Dept of Physics, University of Wisconsin, WI, (boldyrev@wisc.edu)*

<sup>6</sup>*Astrophysics, Department of Physics, University of Oxford, Keble Road, Oxford, OX1 3RH, UK*

<sup>7</sup>*Department of Physics and Electronics, Rhodes University, PO Box 94, Makhanda, 6140, South Africa (ian.heywood@physics.ox.ac.uk)*

<sup>8</sup>*National Radio Astronomy Observatory, Charlottesville, VA, USA, (bcotton@nrao.edu)*

<sup>9</sup>*South African Radio Astronomical Observatory, 2 Fir Street, Black River Park, Observatory, Cape Town, 7925, South Africa, (fernando@ska.ac.za)*

### ABSTRACT

We carry out a population study of magnetized radio filaments in the Galactic center using MeerKAT data by focusing on the spacing between the filaments that are grouped. The morphology of a sample of 43 groupings containing 174 magnetized radio filaments are presented. Many grouped filaments show harp-like, fragmented cometary tail-like, or loop-like structures in contrast to many straight filaments running mainly perpendicular to the Galactic plane. There are many striking examples of a single filament splitting into two prongs at a junction, suggestive of a flow of plasma along the filaments. Spatial variations in spectral index, brightness, bending and sharpening along the filaments indicate that they are evolving on a  $10^{5-6}$ -year time scale. The mean spacings between parallel filaments in a given grouping peaks at  $\sim 16''$ . Modeling of the spacing between the filaments indicates that the filaments in a group all lie on a same plane and are isotropically oriented in 3D space. One candidate for the origin of filamentation is interaction with an obstacle, which could be a compact radio source, before a filament splits and bends into multiple filaments. In this picture, the obstacle or sets the length scale of the separation between the filaments. Another possibility is synchrotron cooling instability occurring in cometary tails formed as a result of the interaction of cosmic-ray driven Galactic center outflow with obstacles such as stellar winds. In this picture, the mean spacing and the mean width of the filaments are expected to be a fraction of a parsec, consistent with observed spacing.

*Keywords:* ISM: magnetic fields, ISM: cosmic rays, radiation mechanisms: non-thermal, plasmas

### 1. INTRODUCTION

Apart from the Sgr A complex where the supermassive black hole lies at the center of the Galaxy, the first hint that the nucleus of our Galaxy harbored energetic activity was the discovery of the prototype magnetized radio filaments in the Galactic center Radio Arc near  $l \sim 0.2^\circ$  more than three decades ago (Yusef-Zadeh, Morris & Chance 1984). Since then, VLA observations have shown linearly polarized synchrotron emission tracing nucleus-wide cosmic ray activity throughout the inner few hundred pc of the Galaxy (Liszt 1985; Yusef-Zadeh et al. 1986; Bally & Yusef-Zadeh 1989; Gray, et al. 1991; Haynes, et al. 1992; Staguin et al. 1998; Lang et al. 1999; Lang, Morris & Echevarria 1999; LaRosa, Lazio & Kassim 2001; LaRosa, et al. 2004; Yusef-Zadeh et al. 2004; Nord et al. 2004; Law, Yusef-Zadeh & Cotton 2008; Pound & Yusef-Zadeh 2018; Staguin et al. 2019; Arendt et al. 2019). MeerKAT observations have recently provided a remarkable mosaic of the inner few degrees of the Galactic center revealing a radio bubble of  $\sim 400$  pc in exquisite detail with  $4'' - 6''$  spatial resolution (Heywood, et al. 2019; Heywood et al. 2022; Yusef-Zadeh et al. 2022). Each of the filaments tracks a source of cosmic rays suggesting high

cosmic-ray flux in the Galactic center.  $\text{H}_3^+$  absorption line observations (Oka, et al. 2019) also indicate high cosmic ray ionization rates permeating the Central Molecular Zone (CMZ) at levels a thousand times that in the solar neighborhood. One of the consequences of the interaction of cosmic ray particles with the gas in the CMZ is to heat the gas to higher temperatures (Yusef-Zadeh, et al. 2013). Multiple observational studies show that warm gas temperatures characterize molecular clouds in the CMZ (Henshaw et al. 2022).

*Chandra*, *XMM* and *NuSTAR* have detected X-ray emission from a handful of nonthermal radio filaments. Five prominent filaments have been studied in detail, G359.89–0.08 (Sgr A-E), G359.54+0.18 (ripple), G359.90–0.06 (Sgr A-F), G0.13–0.11, and G0.173–0.420 (Sakano, et al. 2003; Lu, Wang & Lang 2003; Lu, Yuan & Lou 2008; Yusef-Zadeh, et al. 2005; Zhang, et al. 2014, 2020; Yusef-Zadeh et al. 2021). Unlike the long and distinct radio filaments, there are also several short, linear X-ray features identified within  $6'$  of Sgr A\*, the supermassive black hole at the Galactic center (Muno, et al. 2008; Johnson, Dong & Wang 2009; Lu, Yuan & Lou 2008).

Although numerous models have been proposed to explain the origin of the filaments, there is no consensus on how these filaments are produced (Nicholls & Le Strange 1995; Bicknell & Li 2001; Dahlburg, et al. 2002; Yusef-Zadeh 2003; Ferrière 2009; Banda-Barragán, et al. 2016). Broadly speaking nonthermal radio filament (NRF) models invoke an energetic event or compact source accelerating cosmic rays to high energies (Rosner & Bodo 1996; Shore & LaRosa 1999; Yusef-Zadeh & Wardle 2019) or else a process that involves the environment of the Galactic center hosting high cosmic-ray flux, highly turbulent medium and highly organized large-scale magnetic fields (Boldyrev & Yusef-Zadeh 2006; Thomas, Pfrommer, & Enßlin 2020; Sofue 2020; Coughlin, Nixon, & Ginsburg 2021).

The abundance of NRFs within the radio bubble indicated that some filaments are isolated but others are grouped together (Heywood et al. 2022; Yusef-Zadeh et al. 2022). A statistical study characterizing the mean properties of the spectral index and the equipartition magnetic field of NRFs based on MeerKAT data were recently discussed (Yusef-Zadeh et al. 2022). The mean magnetic field strengths along the filaments ranged between  $\sim 100$  to  $400 \mu\text{G}$  depending on the assumed ratio of cosmic-ray protons to electrons. The large equipartition magnetic field along the filaments is different than large-scale magnetic flux averaged over the entire Galactic center region. This suggests that the magnetic field along the filaments is significantly amplified locally when compared to pervasive magnetic field in this region. The mean spectral indices ( $\alpha$ ) of the filaments, where flux density  $S_\nu \propto \nu^\alpha$ , were also shown to be steeper than supernova remnants (SNRs). This characteristic of the filaments and its wide range in the spectral index variation may indicate different mechanism accelerating particles in the filaments than typical SNRs.

Here we continue our total intensity and spectral index studies but focus on groups of filaments observed throughout the Galactic center. We present images of about 43 groupings of filaments consisting of 174 individual filaments using unfiltered and filtered images. We have not studied single filaments that are not members of any group of filaments. We show a new characteristic of the filaments in that they are spaced equally from each other with the mean value of  $\sim 16''$ . We also determine the mean width span of all filament groupings is  $\sim 27''$ . We interpret that filament separation is due to synchrotron cooling instability. Another possibility that we discuss is an interaction of cosmic-ray driven outflow with an obstacle with a size scale of the width of a filament or a group of filaments triggering filamentation.

## 2. OBSERVATIONS

### 2.1. MeerKAT

Details of MeerKAT observations including spectral index determination of the entire region and the procedure in making high-pass filtering of mosaic images can be found in Heywood et al. (2022) and Yusef-Zadeh et al. (2022). Briefly, the mosaic image is filtered using a difference of Gaussians to smooth out noise and remove large scale backgrounds in order to enhance the visibility of narrow filaments. The narrower, smoothing Gaussian function has  $\sigma = 2.75''$  and the wider, background-subtracting Gaussian function has  $\sigma = 4.95''$ . Unfiltered images have FWHM  $\sim 4''$  resolutions. Point sources in the final filtered image have FWHM  $\sim 6.4''$ , and negative side lobes that are  $< 11\%$  of the filtered peak value. The process reduces the numerical value of the brightness in filament pixels by a factor of  $\sim 0.13$ , with large variations due to the effect of the background removal. This factor is not applied to the filtered image intensities, presented in Figure 2a to 29a, which need to be increased by  $\sim 7.7$ . However, this factor does not effect the calculation of spectral indices. The spectral index is determined using cubes of 16 filtered frequency channels. Pixels lacking sufficient signal are assigned “not a number” (NaN) values, and appear black in later figures. To improve the signal-to-noise ratio (S/N), the median spectral index of each filament is determined from the median of the pixel spectral indices along its length. In cases where an insufficient number of pixels have valid spectral indices, the median

spectra index may be reported as NaN. The statistical uncertainty of the mean spectral index is typically  $\sim 0.1$ , but can drop as low as 0.01 for long bright filaments. Part of the uncertainty may be caused by intrinsic variation of the spectral index, but in most cases it is dominated by measurement uncertainties.

## 2.2. VLA

We used the Karl G. Jansky Very Large Array (VLA) to obtain a higher resolution image of the region toward Sgr C. The observation was carried out at L-band (1–2 GHz) with the array in the most extended A-configuration and centered at Sgr C (J2000  $17^{\text{h}}44^{\text{m}}35^{\text{s}}.0$ ,  $-29^{\circ}29'00''.0$ ) for 2.5 hours. The initial flagging and reference calibration was performed using the VLA casa pipeline8 and processed with the wsclean multiscale clean algorithm with a resolution of  $\sim 1''$ . Further details on the use of the VLA data can be found in Heywood et al. (2022).

## 3. RESULTS

The new MeerKAT data reveal new morphological and spectral details of NRFs. We identified a large sample of prominent groupings of filaments with memberships ranging from pairs to dozens. We define a grouping as a set of filaments with similar orientations, similar curvature or bending, and spatially close to each other. In some cases, the filaments in a grouping converge to a point, shift sideways together, change direction coherently implying that they are parts of the same system of filaments with similar origin. These are distinct from filaments along the line of sight at large physical distances from each other but which appear close in projection. Here, we only focus on some of the most spectacular groupings of filaments and their spectral indices. The results are summarized below.

- Many filaments in groupings are approximately equally separated from each other and run parallel to each other, giving the appearance of a harp. In some groupings, the brightest filament lies at one edge, suggesting harmonics of the brightest filament followed by fainter filaments running parallel to the bright filament. In other cases, the filament lengths in a grouping progressively diminish toward zero.

- Most filaments in a grouping are parallel to each other, change direction coherently, and appear to converge to an external point, similar to the shape of a cometary tail or meteor trail. The filaments in many groupings are bent gently, and some show loop-like structures bending by  $\sim 90^{\circ}$ . These morphological details suggest that grouping filaments are threaded by the magnetic field and have similar origin.

- The spectral index between individual grouping filaments trends between flat (hard) and steep (soft) for short and long filaments. The change in the spectral index, filamentation and morphological changes such as the width, and brightness of the filament give us clues to the evolution of the relativistic electron population along the filaments.

- In some instances, a single filament encounters a compact source or a region of enhanced emission and then splits into two parallel fainter filamentary components. Spectral variations are noted across the length of filaments before and after splitting. This suggests filaments carry a flow of plasma along their lengths and that an interaction with an obstacle such as a stellar bubble or a planetary nebula triggers filamentation. In a grouping with a number of parallel filaments, we explore the possibility that filamentation occurs because of synchrotron cooling instability.

### 3.1. Total intensity and spectral index images of filament groups

Figure 1 shows the MeerKAT mosaic image of Galactic center (Heywood et al. 2022) and the red boxes highlight identified groupings of filaments. With the exception of the Radio Arc near  $l \sim 0.2^{\circ}$ , most prominent groupings lie at negative longitudes. Figures 2 to 29 display structural details of each grouping of filaments in each box as well as their spectral indices. Each of these figures consists of four sub-images. The top panels show the surface brightness using filtered and unfiltered data (a, b). The bottom panels show the median and pixel-by-pixel spectral index images of individual filaments (c, d). Positions of individual compact sources and other locations of interest (discussed below) are marked as blue circles. Because of limited spatial resolution, it is not clear if any of the identified compact sources are related to filaments, nevertheless, the apparent association is suggestive of interaction of compact radio sources with filaments. Opposing pairs of red tick marks overlaid on the filtered and unfiltered images designate the separation between the inner and outer filaments. The mean spacing was evaluated by counting the number of individual filaments. Table 1 tabulates the separations measured for various filament groupings. Nicknames are given to individual groupings based on their appearance, Galactic coordinates ( $l, b$ ) at the center of the tick marks drawn on filtered and unfiltered images, the angular separation between the inner and outer identified filaments, the number of filaments, and the mean separation of individual filaments in columns 2 to 7, respectively. The last column lists the relevant figure number

of enlarged figures as indicated in Figure 1. We identified a number of compact sources and sources of interest, their positions are drawn on figures as blue and red circles, respectively. Table 2 lists the coordinates of sources, where their names and Galactic coordinates ( $l, b$ ) are tabulated in columns 1 to 3. Column 4 identifies whether the source is compact or a position of interest, as drawn as red and blue circles on Figures 2 to 29, respectively. The last column gives the figure number that compact sources are identified.

### 3.1.1. *Figure 2: G358.743-0.215 (The Horseshoe)*

358.743-0.215 with its horseshoe-shaped structure is one of the few filament groupings that is bent substantially and lies along the Galactic plane, unlike typical filaments that run perpendicular to the Galactic plane. The western side of the grouping consists of a single filament, which splits into two components where there is a compact source 358.733-0.229 and enhanced emission along the filament. The split filaments are separated by  $\sim 18''$  and converge to the north suggesting that the magnetic field along the filaments is continuous and is threaded through both separated filamentary components. The spectral index of the brightest region where the filament splits into two loop-like filaments is flatter by  $\delta\alpha \sim 0.16$  than the loops, suggesting that re-acceleration of particles took place in brighter region. If the magnetic field is initially straight, it is possible that large-scale motion of surrounding plasma is responsible for significant bending of the magnetic field along the filament. There is a compact source at the western edge at G358.693-0.227, although it is not clear if it is associated with the filament.

### 3.1.2. *Figure 3: G358.828+0.471 (The Pelican)*

G358.828+0.471, aka the Pelican, was the first example of a group of filaments running parallel to the Galactic plane (Anantharamaiah et al. 1999; Lang et al. 1999). Detailed VLA observations of this grouping detected linearly polarized emission, consistent with synchrotron emission (Lang et al. 1999). Figure 3 shows four separate filaments that run parallel to each other along the  $\sim 7'$  length and  $45''$  width of the Pelican.

The mean spectral index of the individual filaments in the grouping is close to  $\sim -1$ . The spectrum of the western filaments is steeper than the eastern half, suggesting that the western structure is older. We also notice that the filaments become fainter, more diffuse and spread wider towards the west whereas the eastern filaments are bright, have narrow widths and are sharp in their appearance. This is consistent with the spectral index gradient in suggesting that the western half is more evolved. If the magnetic field was initially vertical and perpendicular to the Galactic plane, the large-scale motion of the surrounding plasma in this region has a component along the Galactic plane, bends the magnetic field and runs from east to west. We also note three compact sources at the ends of the filaments in the western half: G358.776+0.454, G358.794+0.479 and G358.798+0.468.

The rotation measure (RM) distribution also shows a gradient with the eastern half having  $RM \sim 500 \text{ rad m}^{-2}$  whereas the western half RMs range between -1000 and -500  $\text{rad m}^{-2}$  (Lang et al. 1999). If the RM gradient is intrinsic, the orientation of the magnetic field along the line of sight must be switching by  $\sim 180^\circ$ .

### 3.1.3. *Figure 4: G359.128+0.634 (The Arrow)*

This grouping consists of three parallel filaments in which the longest and brightest filament extends for  $\sim 30'$ . The brightest filament shows a gentle curvature bending by few degrees toward northwest, becoming brighter, more diffuse and wider in its width. Figure 4b shows diffuse emission between filaments in the NW direction. These morphological details suggest that the bright filament is evolving from SE to NW.

G359.128+0.634 lies in projection at the western boundary of the extended Galactic Center Lobe (GCL) (Sofue & Handa 1984) or at the western edge of the radio bubble (Heywood, et al. 2019). We note a clear change in the brightness of extended and diffuse emission across the long filament. This clear demarcation across the Arrow suggests that it coexists with the western edge of the large-scale Galactic center bubble.

The two brightest filaments in G359.128+0.634 show similar spectral index values,  $\alpha \sim -1.3$  to  $-1.4$ . The compact source 359.072+0.735 lies along the filament and shows a flat spectrum consistent with a thermal source. The deviation from a straight filament toward NW near the compact source is noted. It is not clear if the compact source is a foreground object or is interacting with the long filament.

### 3.1.4. *Figure 5: G359.132-0.296, G359.159-0.111, G359.196-0.474 (The Snake)*

The well-known group of filaments in the Snake with a length of  $\sim 30'$  ( $\sim 70 \text{ pc}$ ), is one of the longest in the Galactic center. Figure 5 overlays three locations where the spacing between the filaments have been measured. Unlike most other Galactic center filaments that exhibit smooth curvature like the Arrow, the Snake is unique in

that it is distinguished by its three different curvatures and two kinks, northern and southern, along its length. It is intriguing that there are two compact radio sources G359.132-0.200 and G359.120-0.265 located to the west of the northern and southern kinks, respectively. Similarly the equipartition magnetic field, which scales with the total intensity, has a maximum of  $\sim 0.15$  mG as it decreases from north to south (Yusef-Zadeh et al. 2022). Faraday rotation measures of 5500 and 1400 rad m $^{-2}$  have been reported to be due to an external and internal medium, respectively (Gray, et al. 1995).

The Snake has a nonthermal radio spectrum with typical spectral index  $\alpha \sim -0.7$ . The region to the north of the southern kink is brighter, and has a spectrum of close to  $\sim -0.6$  and becoming steeper to a value of  $\sim -0.9$  at the southern end. This suggests that cosmic ray particles are more recently accelerated to the north of the northern kink, than to the south of the southern kink.

### 3.1.5. *Figure 6: G359.221-0.129 (The Candle)*

G359.214-0.100 consists of a number of faint filaments and a single bright filament all running vertically. A compact source G359.212-0.087 is detected at the northern end of the bright filament. The northern extension of the bright filament splits into multiple faint components followed by a shell-like structure within which a bright compact source G359.211-0.085 lies (see Figure 6b). The bright vertical filament and the shell-like structure give the appearance of a flaming candle. We also note a number of faint filaments on the eastern side of the vertical filament giving the appearance of a fan. The faint filaments are terminated at a resolved compact source G359.224-0.136 with its bow-shock appearance. The spectral index of G359.221-0.129 is steep when compared to the Snake. The shell-like source and the compact sources have a thermal spectrum.

### 3.1.6. *Figure 7: G359.317-0.430 (The Sausage)*

G359.317-0.430 consists of three components, the brightest and narrowest segment is in the middle and two wider and fainter filamentary structures to the NE and SW. The bright middle section of this filamentary structure with its sausage-like appearance is unresolved but the northeastern and southwestern extensions are split into multiple components. The SW extension splits into two components, becoming fainter, giving the appearance of a two-pronged fork. Two discrete sources, G359.324-0.430 and G359.321-0.431, are detected at the junction where the SW extension of the filament splits. Similarly, the NE extension is wider, fainter, is more diffuse with smoother curvature, and splits at the position of the bright radio source G359.344-0.416 (peak intensity of  $\sim 1.6 \times 10^{-4}$  Jy beam $^{-1}$ ).

The compact sources in the SW, where the filament splits into two, are possibly acting as an obstacle responsible for structural change in the filament; this is suggestive of a flow running along the filament. The change in the brightness and deviations from a straight line also suggests that an interaction is taking place. We note that the spectral index of the bright sausage-like filament is steeper than the filament to the southwest by  $\delta\alpha \sim 0.45$ . This mean spectral index value includes the faint and strong emission, so it is not an accurate estimate of the spectral index of the bright region. We note in Figure 7d, a hint that the spectral index of the bright region is flatter than the faint feature to the SW. This suggests that cosmic ray particles are re-accelerated at the location of the bright sausage-like structure. The characteristics noted in the NE direction can also be explained by the bulk motion of large-scale plasma flow, that is diffuse in NE, compressing the magnetic field along the sausage-like structure and then breaking into two parallel components in SW.

### 3.1.7. *Figure 8: G359.300-0.175 and G359.366-0.140 (The Hummingbird)*

The region to the south of Sgr C (G359.45-0.08) is rich with filamentary structures, lying at the western boundary of the large-scale Galactic center lobe and the radio bubble. Figure 8 exhibits parallel filaments connect to a prominent HII region in the Sgr C complex. The filaments appear to be dragged from Sgr C by large-scale plasma motion with a strong component running SW, away from the Galactic plane. The grouping shows wobbly and diffuse structure closer to the HII region and then straightens while bending by a few degrees to SW at G359.321-0.158, giving the appearance of hummingbird beak. The spectral index of the filaments is somewhat flatter than most nonthermal radio filaments. Chandra observations of this source shows X-ray emission from the region where the filament bends most (Yusef-Zadeh et al. 2007). Spitzer's MIPS image shows a ridge of  $24\mu\text{m}$  dust emission running parallel to the eastern half of the filaments. It is possible that the flatter spectral index of the filament arises from the surface of dust cloud, though is not clear if the two, the filament and the ridge of  $24\mu\text{m}$  emission, are associated with each other.

### 3.1.8. *Figure 9: G359.411-0.709 (The Feather)*

Figure 9 shows a beautiful grouping of two long eastern and western filaments running with similar curvature. This grouping gives the appearance of a feather in which the spacing between the filaments becomes narrower to the north and diverges to the south. The curvature of parallel filaments suggests that they both have similar origin where they converge to the NE. The extension of these filaments to the north appears to converge at a location where a compact source G359.419-0.583 lies. The spectral index of the western, fainter filament is steeper than the eastern filament.

There are two substructures noted along the filaments. One is to the south where the eastern filament splits into two components. This is another striking example of two-pronged forked filament with the junction at the location of a compact source G359.416-0.706. Similar to the Sausage G359.317-0.430, as discussed above (Fig. 7), the compact source may be an obstacle that splits the bright eastern filament into two parallel, fainter filaments with a steeper spectral index. The spectral index variation is consistent with re-acceleration of particles at the junction where the filaments separate. This suggests that large-scale bulk flow is compressing the magnetic field from NE to SW before the flow breaks up into two components after encountering the obstacle.

The second substructure is a distortion along the western filament at 359.420-0.660. A compact source lies  $\sim 14''$  SE of the depression at 359.423-0.664 with a peak intensity of  $36 \mu\text{Jy beam}^{-1}$ . The shape of the distorted filament suggests a wind-blown outflow from the compact source is responsible for distorting the adjacent filament into a cavity. Another possibility is the structure is due to a background contaminating radio source superimposed at the location where the distortion is noted.

### 3.1.9. Figures 10: G359.425+0.043 and G359.446-0.005 (SgrC)

Sgr C is one of the most well-known massive star-forming regions in the CMZ showing thermal and nonthermal radio continuum emission and hosting dense molecular gas (Yusef-Zadeh et al. 2007; Pound & Yusef-Zadeh 2018; Chuard et al. 2018; Martinez 2020). Figure 10 shows the circular-shaped Sgr C HII region and prominent nonthermal vertical filaments on the eastern side where there is a hole in the HII region. The bright vertical filament extends not only to the N but to the S, as discussed below (see Fig. 12). VLA image of the vertical filament at 8 GHz showed  $\sim 4$  knot-like structure along the filament (see Figure 10b of (?) before the filament bends to NW. The spectral indices of the knots along the filament in 10(d) show flatter spectrum than the filament. The vertical filament N of  $b = -0.04^\circ$ , where the brightest knots is noted, consists of E and W filaments running parallel to each other.

The western component is bright and straight, unlike the eastern filament which appears wobbly and appears to be dragged out of the diffuse Sgr C HII region, deviating from the bright filament and curving to NW near  $b \sim 0.0^\circ$ .

The brightest segment of the Sgr C vertical grouping lies between G359.455-0.055 and G359.453-0.033 with an extent of  $\sim 2'$ . The northern extension of the filament from the compact source G359.455-0.055 (saturated in Fig. 10) bends NE by few degrees and becomes brighter by a factor of  $\sim 2$ . This strongly suggests that there is an interaction between the compact source, with a peak intensity of  $\sim 0.3 \text{ mJy beam}^{-1}$ , and the filament. We note that the NW extension of the vertical component of the Sgr C filament is bent again to NW at G359.455-0.033, becomes wider and breaks up into a large number of parallel components with steeper spectrum. We note a bright thermal feature with a hook-shape appearance is oriented parallel to the Galactic plane and crosses the Sgr C filament at G359.439+0.006. A high-resolution  $\sim 1''$  VLA image of the same region is shown in the bottom panel of Figure 10(e) where we note clearly that the direction of the vertical filaments deviate at the intersection where the horizontal structure G359.439+0.006 is noted. In addition, multiple fainter filaments are created to the north of G359.439+0.006. It is most likely that the filamentation is triggered by the interaction of two vertical bright filaments with the horizontal hook-shaped structure, as we have observed in a number of filament groupings. Another example is the northern extension of the Radio Arc where there is ring-shaped structure, as noted in Figure 24, causing filamentation. The mean spectral index of the filaments in Sgr C ranges between  $\alpha \sim -0.5$  to  $\sim -0.6$ .

### 3.1.10. Figure 11: G359.429+0.132 and G359.495+0.188 (The French Knife and the Concorde)

Figure 11 displays three groupings of filaments, one of which is G359.484+0.122, as discussed below (Fig. 13). The red markings show where three groupings are located. G359.429+0.132 lies to the right of the image and resembles a French knife. This structure consists of a loop-like structure that bends by  $\sim 90^\circ$  and a bright vertical filament. Low-resolution observations had detected this grouping at 6 and 20 cm, called C6 and C7 (Yusef-Zadeh et al. 2004; Law, Yusef-Zadeh & Cotton 2008). The horizontal component runs along the Galactic plane. Adjacent to the bright vertical filament, two additional fainter, but longer filaments run parallel to the bright vertical filament. The vertical component of G359.429+0.132 shows a pattern noted in a number of filament groupings where multiple parallel filaments with different brightness, length and spectral index run adjacent to each other, as shown Figure 11. The

spectral index of the vertical filaments is steeper for the fainter filaments. We also notice that the loop-like filament has a flatter spectrum than the vertical filaments by  $\delta\alpha \sim 0.3$ . Bending of the loop-like filament is perhaps caused by a large-scale plasma motion in the NW direction.

Lastly, G359.495+0.188, which is located to the NE of Figure 11, shows three filaments with spacing that becomes narrower toward the north giving the appearance of the Concorde aircraft. Again, the structure of G359.495+0.188 is similar to converging fragmented cometary tail-like pattern noted in a number of filament groupings.

3.1.11. *Figure 12: G359.504-0.321, G359.399-0.213, and G359.397-0.187 (The Cataract, the Forceps and the River)*

The grouping of filaments in G359.504-0.321 appears like a cataract, as shown in Figure 12, and is characterized as a broad grouping of closely-spaced filaments that are difficult to distinguish because of limited resolution, confusion, and/or intrinsic diffuse emission. This system consists of both diffuse and filamentary structure. The morphology of the cataract system is unusual in that the northern part of the system is wider and more diffuse than the south. The faint filaments run parallel to each other, shift together to the east and to the west suggesting that the magnetic field of the filaments change direction coherently implying that they are parts of a larger magnetic structure. The large-scale structure consists of three parallel components separated by gaps with a width of  $1 - 2'$  with weaker emission between them. One gap is prominently shown to the south of the extended cometary source G359.467-0.171. The spectral index distribution of the Cataract grouping appears to be flatter than typical steep spectrum of filaments, as shown in Figure 12d. This perhaps suggests that they are relatively younger or that the relativistic electron population has recently been re-accelerated.

The exact relationship between the Cataract and the Sgr C HII region is not clear but there appears to be an association with the prominent nonthermal Sgr C filaments. We note that a narrow and long filament that is clearly the southern extension of the vertical bright Sgr C filaments, bends  $\sim b = -0.107^\circ$  and continues to the south. Another bend is seen on the western edge of the extended cometary HII region at G359.467-0.171. The wavy pattern of the filament has a wavelength of  $\sim 15'$ .

The northern extension of this grouping is a single, slightly bent filament that merges with the Sgr C filament, as discussed above (Fig. 10), and displays a wavy pattern which appears to be distorted near the Galactic equator and the cometary HII region. The southernmost extension of this single filament becomes brighter, narrower in its width and bends at the closest approach to the cometary feature. This suggests that there is an interaction because the HII region shows a linear feature at its western edge and appears to be torn by the filament. Furthermore, the variation of the spectral index from north to south shows flattening of the spectrum, implying re-acceleration of particles along the filaments to the south of the cometary feature. These support a picture that these features are embedded in a large-scale flow directed to the south of the Galactic plane.

Figure 12 also shows another filament grouping G359.399-0.213 with an appearance of two-pronged forceps running vertically. We note a curious structure consisting of two filaments that are separated by  $18''$  and run vertically to within a degree perpendicular to the Galactic plane. This faint and narrow filaments give the appearance of a narrow river. The River grouping, (Fig. 8), lies to the north of the Forceps. This vertical filament splits into two fainter diverging components at G359.401-0.238 along its northern extension. The spacing between these two components is similar to that of filaments in the River. It is not clear if these two structures are associated with each other. The southern extension of the filament becomes brightest with a kink at G359.405-0.259. The spectral index of the Forceps is  $\alpha \sim -0.59$ .

3.1.12. *Figure 13: G359.484+0.122 (The Bent Harp)*

G359.484+0.122 is a remarkable grouping consisting of five regularly spaced filaments with the appearance of a bent harp. A trend is noted between the length of the filaments and their brightness. These harp-like systems ordered by length have previously been described by Thomas, Pfrommer, & Enßlin (2020). The spectral index distribution shown in Figure 13c,d suggests another trend between the length of the filament and the steepening of the spectral index. Shorter filaments have flatter spectral index values. The regular spacing between the filaments becomes narrower to the SW to the point that the grouping appears to converge at 359.439+0.103 shown in the wider view of Fig. 11. The SW extension of the filaments appears sharper and narrower than their NE extension. It is possible that filamentation occurred as a result of an interaction in which multiple components are produced. Bending of the filaments can also be explained in this picture by assuming that an obstacle is moving through the cosmic-ray driven nuclear wind. We also note a compact source at G359.485+0.121 with a peak intensity of  $\sim 60 \mu\text{Jy beam}^{-1}$  that lies between two of the longest filaments as well as a compact source at G359.475+0.127 adjacent to the shortest filament. Lastly, we note

a compact source along the longest filament at G359.491+0.121 with a peak intensity of  $\sim 12 \mu\text{Jy beam}^{-1}$ . The NE extension of this filament beyond the compact source G359.491+0.121 is split into two components (see Fig. 13b). Again, the compact source may act as an obstacle embedded in a large-scale flow from SW to NE and be responsible for splitting the long filament into two components.

A bright source G359.522+0.097 with a peak intensity  $\sim 300 \mu\text{Jy beam}^{-1}$  is also noted to the SE of the image. This bright source is resolved into an asymmetric shell and a short cometary tail running to the NE. The spectral index of this source is consistent with an HII region. The orientation of the cometary HII region and the regularly spaced filaments both suggest large-scale flow in the direction away from the Galactic plane.

### 3.1.13. *Figure 14: G359.359.520+0.237 (The Ripple)*

G359.520+0.237 is another group of filaments with a length of  $\sim 0.3^\circ$ , as shown in Figure 14. The figure shows contrasting details between the bright, distorted structures in the SE and straight, faint filaments in the NW. The NW end of the grouping shows multiple straight filaments running parallel to each other. However, the grouping is distorted toward the SE end, exhibiting ripple-like appearance on the brightest side of the grouping. The ripple-like distortions are brighter than the straight NW filaments by a factor of  $\sim 10$ . The cause of the ripple is thought to be an interaction with clumps of a molecular cloud in the SE (Bally & Yusef-Zadeh 1989; Staguhn et al. 1998). We also note splitting of the bright filament in the SE into two distorted components at a junction with a compact source at G359.557+0.140. This appearance is reminiscent of other filament groupings showing filamentation at a junction where there is a compact source.

Earlier polarization and spectral index studies of the brightest segment of this grouping indicate that the intrinsic magnetic field runs along the filament (Yusef-Zadeh, Wardle & Parastaran 1997) and the spectral index at multiple frequencies is between -0.5 and -0.08 (Yusef-Zadeh et al. 2004; Anantharamaiah et al. 1991; Law, Yusef-Zadeh & Cotton 2008). Figure 14d shows spectral index variations along the filaments. The region near the ripple shows a flatter spectrum than to the NW suggesting that re-acceleration has occurred. This behavior is consistent with an interaction hypothesis, perhaps with a molecular clump (Bally & Yusef-Zadeh 1989; Staguhn et al. 1998). It is possible that the NW filaments were initially extended to the SE along its straight direction before a molecular clump interacted with the filaments and distorted its structure. The rotation measure between -4200 and -3700  $\text{rad m}^{-2}$  is reported to vary on scales of several arcseconds, implying that the ionized, magnetized medium is less than 0.1 pc thick (Yusef-Zadeh, Wardle & Parastaran 1997). This is another example in which filamentation and distortion of straight filaments occur at a junction where there is an obstacle implying that there is flow of material along the Ripple. Lastly, another structure to the NE, G359.563+0.249, consists of two filaments is better seen, and discussed, as part of the next figure.

### 3.1.14. *Figure 15: G359.640+0.308, G359.625+0.298, and G359.563+0.249 (The Broken Harp and the Edge-on Spiral)*

Figure 15 shows a grouping of filaments that appear like a broken harp or two harps that are crossing each other. G359.640+0.308 runs roughly perpendicular to the Galactic plane with mean spacing of  $15.5''$  whereas G359.625+0.298 is tilted by  $10\text{-}20^\circ$  with mean spacing of  $10.6''$ . Spectral indices of vertical and tilted filaments show a relatively flat distribution, which is unusual when compared to typical steep spectrum of filaments found in this region (Yusef-Zadeh et al. 2022). Low-resolution studies of this region indicate spectral index values ranging between -0.3 and -0.1 (Law, Yusef-Zadeh & Cotton 2008), consistent with some of the filaments shown in Figure 15c,d. The diffuse emission between the filaments may have contributed to spectral index estimates measured at low resolution.

We also note two parallel filaments G359.563+0.249 to the SW (also present in Fig. 14) that appear to be twisted about each other, giving the appearance of an edge-on Spiral. Figure 15b shows excess diffuse emission above the background is between the filaments suggesting that the two filaments are physically related to each other. G359.563+0.249 has a steep spectrum ( $\alpha \sim -0.99$ ) compared to the adjacent Broken Harp.

### 3.1.15. *Figure 16: G359.687-0.435 and G359.702-0.517 (The Waterfall and the Hilltop)*

Figure 16 shows another striking grouping of filaments, G359.687-0.435, which resembles a waterfall, and consists of at least six filaments with a mean separation of  $18''$ . The brightest filament lies at the western edge. The fainter filaments run parallel to each other, shift to the east near  $b \sim -0.43^\circ$  and then to the west near  $b \sim -0.45^\circ$ . This suggests that the magnetic field of the filaments change direction coherently implying that they are parts of a large-scale magnetic structure. The spectral index of the grouping is flatter where thermal and diffuse features lie to the north, and becomes steeper to the south.

The extension of the filaments to the N and NE shows that this grouping fades out and becomes confused with the strong thermal background along the Galactic plane. The remarkable morphology of this grouping suggests that diffuse structure is dragged out of the Galactic plane by a large-scale flow, becoming filamentary and forming a network of equally spaced vertical filaments running to the south.

There is a diffuse circular-shaped structure centered on an extended, thermal HII region G359.734-0.409, having a flat thermal spectrum (not marked in Table 2; Fig. 16c,d). The grouping of parallel filaments runs on one side of G359.734-0.409 which itself is edge-brightened on the side facing the waterfall filaments. The asymmetry of the HII region maybe explained by the relative motion of the circular-shaped HII cloud, acting as an obstacle, with respect to the direction of cosmic-ray driven wind arising from the Galactic plane. This grouping shows similar morphology to that of Cataract G359.504-0.321 (Fig. 12).

Another system of filamentary structure G359.702-0.517 lies to the south of the Waterfall consisting of a long and bright structure with the appearance of a hilltop, as shown in Figure 16. The bright filament is surrounded by three additional faint filaments projected on its sides. The spectral indices of the filaments in G359.702-0.517 is  $\sim -0.5$  which is flatter than steep spectrum of typical filaments with  $\alpha < -1$ .

### 3.1.16. *Figure 17: G359.738-0.792 (The Knot)*

Figure 17 shows an example of two entangled filaments that appear to twist about each other in an elongated knot-shaped structure with an extent of  $\sim 0.6'$ . The bright segment of the filament to the south splits into two at G359.729-0.811 and then rejoins at G359.734-0.801. The spectral index variation, bending and brightening of the filaments near the knot indicate that G359.738-0.792 is where the intersecting filaments are interacting and where re-acceleration of cosmic ray particles is taking place. Two compact sources are noted at one end of the eastern filament at G359.748-0.781 and 359.746-0.784.

### 3.1.17. *Figure 18: G359.808+0.130 and G359.717+0.228 (The Flamingo and the Eyebrow)*

Figure 18 shows a group of filaments where two bright, gently curving filaments bend and break up into multiple components along their NW and SE extensions. This complex group gives the appearance of a Flamingo that is standing on one leg, perpendicular to the Galactic plane. The NE extension is bent by about  $\sim 10^\circ$  and deviate from each other at G359.758+0.198 where there is no obvious compact source. The spectral index of the northern component of the deviated filament is flatter than the that of southern component by  $\delta\alpha \sim 0.2$ .

The northern extension of the Flamingo leg near a source G359.808+0.117 breaks up into multiple filaments running to the NE. The spectral index distribution indicates that the Flamingo has a relatively flat spectrum compared to typical filaments with  $\alpha < -1.0$ . The characteristics of this grouping is similar to the Ripple where large-scale bending, brightening and spectral index variation are detected. We note an isolated CO clump at G359.822+0.107 (Schuller et al. (2021)) at the southern end of the grouping suggesting that the distortion and brightening of the grouping is due to a physical interaction with this clump.

At the SW corner of the image, a grouping with the appearance of an eyebrow is noted. This consists of two filaments, one on top of each other, running with the same curvature suggesting that they are related to each other. The top filament breaks up into multiple components whereas the bottom filament is a single bright filament with flatter spectral index than the top filament. The tendency that filaments that are longer and fainter have steep spectral index values is consistent with those of the Harp, as discussed below. We note a compact source G359.886+0.102 at the eastern end of the the Eyebrow where the filaments converge. It is not clear if this pp is associated with the Eyebrow.

### 3.1.18. *Figure 19: G359.890-0.289 (The Cleaver)*

G359.890-0.289 is located in a rich region of the Galactic center hosting a large concentration of groupings and isolated filaments criss-crossing each other, shown in Figure 19. A bright single filament to the NW with multiple fainter filaments running to the SE parallel to each other. The width of the single filament thickens from  $\sim 4''$  to  $\sim 7''$  and brighter by a factor of 5. The grouping of filaments and a square-shaped diffuse structure to the SE gives the appearance of a cleaver. The SE extension of the bright filament bends by a few degrees at a bright unresolved compact source G359.874-0.264. A more detailed close-up of this unresolved compact source indicates a faint filament splitting into two components running from NW to SE. The spectral index of the bright filament is  $\alpha \sim -1.13$  and that of the square-shaped structure is consistent with being thermal. There is no obvious variation in the spectral index along the long filaments in the grouping. The decreasing sharpness and thickening of the width of the filament,

deviation of parallel filaments, bending, and splitting of the filaments from NW to SE all suggest that the grouping is evolving and supporting a picture that these features are embedded in a large-scale flow directed to the south of the Galactic plane.

We also note to the NE, there is a striking head-tail cometary source which consists of a bright compact thermal source at one end of G359.950-0.259 and an elongated tail. The narrow tail becomes brighter by a factor of five and thicker by a factor of two from NE to SW. The tail is also split into two faint components near G359.921-0.283. The spectral index of the narrow segment of the tail has a flat spectral index but becomes steep  $\alpha \sim -0.71$  where the tail is brightest. These characteristics suggest that cosmic-ray electrons are populated close to the source which is embedded in a large-scale flow.

### 3.1.19. *Figure 20: G359.851+0.374 (The Harp)*

G359.851+0.374 is the best example of harp-like structure in which all the strings run perpendicular to the Galactic plane and show no visible signs of distortion with the exception of the westernmost filament with its gentle concave bend, as displayed in Figure 20. The initially parallel filaments appear to converge for some pairs either to the north or to the south. The morphology of this grouping is similar to the Radio Arc where a number of parallel filaments with different lengths run perpendicular to the Galactic plane (see Fig. 23). The harp-like group of filaments are ordered by their lengths (Thomas, Pfrommer, & Enßlin 2020) and diffuse emission is detected from the regions between the filaments (see Fig. 20b). Low-resolution radio observations of G359.851+0.374 (source N10 in Yusef-Zadeh et al. (2004)) had previously been detected with the VLA at multiple frequencies (LaRosa, Lazio & Kassim 2001; Yusef-Zadeh et al. 2004; Law, Yusef-Zadeh & Cotton 2008) before MeerKAT data became available (Heywood, et al. 2019).

At the leading edge of the Harp where the shortest filament is detected, there is a compact source at G359.837+0.375 with a peak intensity of  $25 \mu\text{Jy beam}^{-1}$ . Four of the shortest filaments appear to have a compact source at the southern end of the filaments G359.841+0.366, G359.844+0.358, G359.848+0.298, and G359.851+0.293. It is not clear if these sources are associated with the filaments or they are background radio sources. We also searched for compact sources to the northern end of the filaments but found only one compact radio source. It is perhaps suggestive that the southern compact sources are associated with the Harp, thus supporting a picture in which the Harp is embedded within a large-scale flow driven away from the Galactic plane.

Another striking result is the spectral index distribution of harp filaments, as shown in Figure 20c,d. There is a tendency that the filaments with the longest lengths have steeper spectra. If such a correlation exists between length and spectral index and assuming that the spectral index traces synchrotron cooling time scale, then it implies that cosmic ray particles in short filaments are younger than in the longer filaments.

### 3.1.20. *Figure 21: G359.992-0.572 (The Comet Tail)*

The grouping G359.992-0.572 seen in Figure 21 consists of six linear structures diverging towards the NW, resembling a fragmented comet tail. The mean angular spacing of the filaments in G359.992-0.572 is  $27.5''$  (Fig. 21) which is relatively large compared to the mean angular spacing of  $\sim 16''$  found towards all groupings (see below). The brightest filament in the grouping branches out into two fainter components at two locations in the NW and SE at G359.992-0.555 and G0.023-0.626, respectively.

We also note three compact sources at the SE ends of the grouping G0.030-0.660, G0.034-0.661 and G0.045-0.668. The spectral index of individual filaments in the grouping vary and show steep spectra. This is consistent with a trend that the filaments with steeper spectral indices lie at high latitudes (Yusef-Zadeh et al. 2022).

### 3.1.21. *Figure 22: G0.138-0.299 and G0.172-0.423 (The Radio Arc S.)*

The filament grouping Radio Arc S-1, G0.138-0.299, is shown in Figure 22 and is labelled S5 in (Yusef-Zadeh et al. 2004). The grouping lies towards the eastern boundary of a diffuse, large-scale linearly polarized Eastern Galactic Center Lobe or the radio bubble (Tsuboi, et al. 1995; Heywood, et al. 2019). The northern extension of this grouping is associated with the Radio Arc, as discussed below (see Fig. 23). The grouping of the Radio Arc has a lateral span of  $\sim 249''$ . The bright filaments in the Radio Arc become faint and diffuse toward southern latitudes. At the eastern boundary of diffuse structure lies a long, bright filament at an oblique angle to the Radio Arc. This grouping, G0.172-0.423, runs vertically for more than  $0.3^\circ$  and is one of the few long filaments that has an X-ray counterpart with an extent of  $\sim 2'$  detected along the brightest segment (Ponti et al. 2015; Yusef-Zadeh et al. 2021). Spectral index distribution of this region indicates that the filament spectra at more negative latitudes are steeper than in the

Radio Arc. This is consistent with single-dish measurements indicating that the extensions of the Radio Arc away from the Galactic plane have steeper spectra than close to the plane (Tsuboi, et al. 1995).

### 3.1.22. *Figure 23: G0.160-0.115 (The Radio Arc)*

Figure 23 shows a segment of one of the longest and most well-known filament groupings associated with the Radio Arc, a prototype magnetized radio filament (Yusef-Zadeh, Morris & Chance 1984). The southern extension of this grouping was discussed above (Fig. 22). This grouping consists of the largest number of filaments, 17, that are parallel to each other and run perpendicular to the Galactic plane with average spacing of  $17''$ . Its polarization, rotation measure and spectral indices have been measured (Paré et al. 2019) indicating that intrinsic magnetic field runs along the filaments. The spectral index of individual filaments in the Radio Arc is flat when compared to other Galactic center filaments, as noted in Figure 23c,d. The Radio Arc's unusual spectral index values are consistent with earlier measurements using wider frequency bands at multiple frequencies (Yusef-Zadeh et al. 1986).

### 3.1.23. *Figure 24: G0.168+0.142 (The Ring)*

Figure 24 shows a grouping of nonthermal filaments surrounding a ring-shaped structure G0.17+0.15 (Yusef-Zadeh & Morris 1988). The southern extensions of the filaments run into the Radio Arc, as discussed in the previous section. G0.17+0.15 is a dusty HII region embedded within the highly polarized radio lobe of the Galactic center (Sofue & Handa 1984; Tsuboi, et al. 1995) where a number of radio filaments meander through the HII region, as shown in Figure 24.

A detection of a hydrogen recombination line with a radial velocity exceeding  $130 \text{ km s}^{-1}$  has been reported toward the ring (Royster et al. 2011). The filaments to the south of the HII region are generally brighter and sharper compared to those to the north. There are 7 harp-like filaments distributed to the south of the ring G0.17+0.15 with mean spacing of  $16.2''$ , which is larger than that of the  $12''$  filament spacing in the Radio Arc. The spectral index of the filaments in the Ring is flat but slightly steeper than those found toward the Radio Arc G0.160-0.115. The interaction of nonthermal filaments with a thermal HII region G0.17+0.15 is very similar to two HII regions, G359.467-0.171 and G359.439+0.006, noted to the south and north of the Sgr C HII region, as discussed above (Figs. 12 and 10), respectively. In both circumstances, the filaments appear to change their characteristics as a result of an interaction with HII regions.

### 3.1.24. *Figure 25: G0.228+0.812 (The Space Shuttle)*

Figure 25 shows a group of three filaments that appear to converge to a single bright filament to the north near a compact source at G0.225+0.843. The structure of the filaments resembles Shuttle rocket with boosters on the sides. These filaments follow similar pattern noted previously in fragmented cometary tail-like groupings in which the separation between the strings decrease, giving the appearance of converging filaments. We note a compact source at G0.226+0.792, with a peak intensity of  $53 \mu\text{Jy beam}^{-1}$  at the southern end of one of the side filaments. This group of filament lies at the easternmost edge of the large-scale Galactic center bubble and along the northern extension of the Radio Arc. Figure 25c,d indicate that fainter filaments to the south have steeper spectral indices than the bright filament to the north away from the Galactic plane.

### 3.1.25. *Figure 26: G0.288-0.259, G0.306-0.273, and G0.297-0.266 (The Porcupine)*

Figure 26 shows two systems of fragmented cometary tail-like structures, G0.228-0.259 and G0.306-0.273, with mean spacings  $6.8''$  and  $14.3''$ , respectively. We note that the longest filaments lie at the edges of these two systems. The mean spacing of the combined grouping G0.297-0.266 is estimated to be  $10.5''$ . This group of filaments gives the appearance of of porcupine quills converging to a bright compact source toward NW at G0.264-0.197 with a peak intensity of  $1.5 \times 10^{-4} \text{ Jy beam}^{-1}$ . The spectral indices of individual filaments are fairly flat with typical values of  $\sim -0.2$  similar to the Radio Arc.

### 3.1.26. *Figure 27: G0.405-0.277 (The Contrail)*

Figure 27 shows a group of filaments which consists of two parallel filaments lying on top of each other. The grouping appears like a contrail of a jet running diagonally. The bright top filament is split into two components at a position G0.420-0.297. The change in the brightness and deviations from a straight line is also noted at this junction. The long bottom filament is very faint in the middle and then becomes bright by a factor of few along the NW and SE directions. The positions at which the filament becomes brighter to NW and SE are G0.421-0.290 and G0.443-0.324, respectively. Spectral index maps show steeper values for the top filament than the bottom filament.

### 3.1.27. *Figure 28: G0.687+0.147 (The Bent Fork)*

Figure 28 shows a loop-like filamentary structure that splits into two filaments, giving the appearance of a bent 2-pronged fork, with filament spacing of  $7.5''$ . At the junction where the eastern filament splits at a location G0.697+0.148, the brightness increases from  $\sim 0.2$  to  $\sim 0.8$  mJy beam $^{-1}$ . At the junction where typical filaments split into multiple components, a compact source or enhanced emission is generally detected. This source is elongated and runs in the same direction as the filaments. As such the resolved structure shows clear evidence that the filament is resolved into two components at the bright and extended juncture and is unlikely to be due to a background source along the line of sight. In addition, the spectral index of the elongated structure appears to be flat compared to the rest of the filaments. These characteristics are very similar to those of the Horseshoe (see Fig. 2) show clear signatures that 359.697+0.148 is physically associated with the grouping and is responsible for splitting the filament and re-accelerating particles.

### 3.1.28. *Figure 29: G0.859-0.597 (The Meteor Trail)*

Figure 29 shows a vertical filament running perpendicular to the Galactic plane and gives the appearance of a meteor trail. The filament breaks up into two components and diverges to the south, away from the Galactic plane. We also note that split filaments show slight curvature to the east. The spectral index is steep and is consistent with filaments at high latitudes having steeper spectral index than those closer to the Galactic plane.

## 4. DISCUSSION

We have studied the detailed morphology and spectral index distributions of close to 40 prominent groupings of filaments in the Galactic center region. The dominant morphology of the groupings that stands out can be characterized as multiple filaments that either run parallel to each other (harp-like), converge to a point (fragmented cometary tail-like), or bend together and form a partial loop. In some cases, a group of filaments such as the Waterfall, Cataract and Hummingbird appear to be dragged out from an HII region and then turning into long, narrow and parallel filaments. In almost all filaments in groupings, we note deviations from a straight verticality running perpendicular to the Galactic plane. We determine below the characteristic size scales associated with the spacing between filaments in a grouping and the width span of groupings, thus providing constraints in the geometry of the filaments. We will then discuss the origin of filamentation as a consequence of either the interaction of Galactic center wind with obstacles or as synchrotron cooling instability in the Galactic center ISM.

### 4.1. *The Geometry of the filaments*

To characterize the structure of groups of filaments, we select 43 cross sections where the mean separation of the filaments is calculated simply as the total span of the cross section divided by the number of spacings. The cross sections are chosen at one or two locations in each grouping where the filaments are well defined. However in some cases, filaments may be very faint or poorly resolved, and the number of filaments may be undercounted (and the separations overestimated). The results are listed in Table 1.

The mean angular separation of the filaments in groupings typically falls in the range  $10 - 22''$  with peak value of  $\sim 16''$  (0.6 pc). Outliers extend up to  $\sim 50''$ . The spacing between any two filaments in a given grouping varies slightly. In groupings with a large number of filaments, the spacing varies by a factor of two.

Figure 30a shows a histogram of the filament spacings. This histogram which has used a sample of 43 grouping cross sections is fitted by a Gaussian with a peak of  $16''$  ( $\sim 0.65$  pc at the 8 kpc Galactic center distance). Large spacings are outliers and could suffer from a lack of sensitivity and confusion. Lack of counts at small angular sizes, as shown in Figure 30a, is likely due to limited spatial resolution  $\sim 6''$ . We also determined the widths of filament grouping or “spans” giving a mean value of  $\sim 27''$  ( $\sim 1.1$  pc). This is the size scale on which filaments are bunched together in a grouping. A histogram of spans of individual groupings is shown in Figure 30b. The peak of the Gaussian is  $\sim 27''$  which corresponds to  $\sim 1.2$ pc.

These angular scales (and the implied linear scales) are new physical parameters that characterize the population of Galactic center filament groupings. The linear separation of the filaments assumes that all filaments are on the plane of the sky. We modeled and reproduced the observed spacing distribution of filament spacing by considering that the filaments have randomly distributed inclinations with respect to the line of sight assuming that the filaments are strand-like (so are not sheet-like structures viewed edge-on). They are arranged in regularly spaced comb-like structures viewed at random inclinations. Then, the observed distribution of the spacings between adjacent 1D filaments is projection of their true spacings onto the plane of the sky.

As described in the appendix, the distribution of apparent spacings for  $h$  for an isotropically oriented population of filament groupings with a single true spacing  $h_0$  is:

$$P(h|h_0) = \int_0^{2\pi} P(\phi, h) d\phi = \begin{cases} \frac{2/\pi}{\sqrt{h_0^2 - h^2}} & \text{when } h < h_0, \\ 0 & \text{otherwise.} \end{cases} \quad (1)$$

This distribution is plotted in Fig. 31a. The significant tail extending towards zero spacings arises because of the large solid angle subtended by highly-inclined viewing angles (i.e. with  $\theta \approx \pi/2$ ).

Then, for a probability distribution  $P_0(h_0)$  of true spacings, we obtain the in-sky distribution

$$P(h) = \int_0^\infty P(h|h_0)P_0(h_0) dh_0 = \frac{2}{\pi} \int_h^\infty \frac{P_0(h_0) dh_0}{\sqrt{h_0^2 - h^2}}. \quad (2)$$

In figure 31b, we show the predicted spacings for a log-normal distribution of the true spacings  $P_0(h_0)$  (blue dashed line).

$$P_0(h_0) = \frac{1}{\sqrt{2\pi} \sigma h_0} \exp\left(-\frac{\ln^2(h_0/a)}{2\sigma^2}\right). \quad (3)$$

with  $a = 20''$  and  $\sigma = 0.2$ , illustrate values chosen so that  $P(h)$  is similar to the observed spacing counts. It is clear that while projection effects reduce the mode of the intrinsic distribution somewhat, the largest effect is to double the 16" FWHM of the true distribution.

#### 4.2. A Causal origin of filamentation

One key question is the origin of the filamentation observed in groupings of Galactic center filaments. One possibility is that a single filament was split by an obstacle into multiple filaments, which then diverge and become more diffuse, as shown in Figures 2, 7 and 9. In this picture, an obstacle sets the length scale of the separation between the filaments as well as the size of the bundle of filaments. Filamentation implies a bulk plasma flow along a filament if it is to break up into multiple filaments at the interaction site. One model that we have explored in the past to explain the origin of the filaments is that nonthermal radio filaments arise through the interaction of the cosmic-ray driven outflow from the disk of the Galactic center and the termination shock of an embedded mass-losing star (Yusef-Zadeh & Wardle 2019). This is analogous to the interaction of the solar wind interacting with obstacles, such as comets, Earth and Mars. In these cases, the solar wind drapes and sweeps over embedded sources in the solar system. Many groupings show diverging filaments from a point which is similar in appearance to fragmented cometary tails.

One of the implications of a scenario in which cosmic-ray driven wind interacts with an obstacle is a flow of plasma along the filaments with similar speed to that of the surrounding large-scale cosmic-ray driven outflow. This characteristic combined with decreasing sharpness and increasing thickening along the filaments suggest that the relativistic electrons on one end are re-accelerated, and then cool as they propagate along the filament. In this picture, the variation of the spectral index can be used to make an estimate of the flow speed of plasma. To this end, the gradients in the spectral index,  $d\alpha/ds$ , were measured as a function of distance,  $s$ , along 191 of the longest filaments. This selection include filaments that are greater than 165" in length and are generally bright. Gradients are estimated using weighted linear fits between  $s$  and  $\alpha$ . The weights are uniform for intensities  $I > 10^{-4}$  Jy beam $^{-1}$ , and are taken to be proportional to  $I^2$  at fainter levels. A negative gradient indicates a steepening spectral index as a function of  $|b|$ , i.e. with increasing distance from the Galactic plane. There is seldom an obvious linear gradient along a filament, but by measuring gradients in many filaments we can assess if there is any general trend in the population of filaments. The histogram of measured gradients is shown in Figure 32.

Using the mean variation of the spectral index along the filaments,  $-1.1 \text{ deg}^{-1}$ , the mean spectra index  $\alpha \sim -0.83$ , and the mean equipartition magnetic field,  $\sim 100$  to  $400 \mu\text{G}$  depending on the assumed ratio of cosmic-ray protons to electrons, we estimate the mean cooling time of the population of cosmic ray particles to be  $\sim 0.5 - 2.7 \times 10^5$  yr. For filaments with lengths ranging between  $\sim 5 - 30\text{pc}$ , the flow speed is estimated to be about  $\sim 100 \text{ km s}^{-1}$ , assuming that shorter filaments have stronger magnetic field. This is suggestive of plasma flow streaming along filaments rather than diffusion.

### 4.3. A Radiative instability origin of filamentation

There are a number of groupings of multiple filaments that don't converge to a point and do not appear to show an interaction with an obstacle, such as the Harp and the Radio Arc, as shown in Figures 20, 23, respectively. One possibility is that filamentation results from synchrotron cooling instability (e.g., Simon & Axford 1967). In this picture, the initial cosmic-ray pressure has to at least be comparable to the magnetic pressure. The instability proceeds as follows: synchrotron losses lower the relativistic particle pressure in a magnetized region, which is then compressed by the surroundings, increasing the field strength. This drives further losses and ongoing compression. To be effective, this picture requires that particles lose energy within a few thousand years implying that the filaments initially had a significant population of TeV electrons emitting X-ray synchrotron radiation. Alternatively, the ISM needed to be permeated by diffuse X-ray synchrotron emission providing a reduction in cosmic-ray pressure to locally trigger the instability. It turns out that this instability causes filamentation on a scale of  $\sim 0.5$  pc, as discussed below. So, it is possible that both cooling instability and an interaction of nuclear wind with obstacles generating X-ray synchrotron emission operate in the Galactic center.

The cause of filamentation could be due to synchrotron cooling instability taking place in the magnetized tail generated from the interaction of cosmic-ray driven nuclear wind with an obstacle (Yusef-Zadeh & Wardle 2019). The magnetic field in the filaments is relatively strong compared to the magnetic field in the diffuse region. The lengths of the filaments and the scales on which some of the filaments are bent are indicative of the scales of external plasma motion. It is therefore reasonable to assume that the magnetic-field energy in the filaments is comparable to the rms energy of the plasma motion, which gives an estimate for the magnetic field strength in filaments  $B \sim 0.1$  mG, consistent with minimum energy inferred from radio synchrotron emission (Yusef-Zadeh et al. 2022). The regions of enhanced magnetic field where filaments originate may be created due to plasma compression or magnetic line stretching in colliding, shearing flows, or in a plasma stream interacting with an obstacle. The same regions may be responsible for the electron acceleration, as they may contain shocks or sites of magnetic reconnection (Drake, Swisdak, & Fermo 2013; Guo et al. 2020).

As discussed above, the presence of multi-filament substructure in many radio filaments may indicate that their origin is governed by the so-called cooling instability (e.g., Simon & Axford 1967). Indeed, let us assume that in the regions where magnetic field is amplified, a significant fraction of plasma pressure is provided by ultra-relativistic electrons, while the plasma mass is dominated by the protons. Then plasma compression in the field-perpendicular direction will lead to amplification of the magnetic field, which in turn will lead to enhanced synchrotron radiation, and as a result, to electron cooling and stronger compression.

As demonstrated in (Simon & Axford 1967), the growth rate of the instability increases at smaller scales. The maximal growth rate is approximately the inverse synchrotron cooling time,  $1/\tau$ . This growth rate is achieved at the wavelength  $\lambda \approx \pi v_s \tau$ , where  $v_s$  is the speed of sound in the medium, and it remains at roughly the same value at even smaller wavelengths, that is, it is almost independent of the scale there.

We now estimate whether the cooling instability may be consistent with the observational width of the filaments, which are on the order of  $\sim 10^{18}$  cm. We assume that the ultra-relativistic electrons have a power-law distribution over energies, so that their number density scales with the gamma factor as  $n(\gamma)d\gamma = n_0\gamma^{-p}d\gamma$ , with  $p > 1$ . Assume that the largest energy of the distribution corresponds to  $\gamma_*$ . Then the total energy density of such cosmic ray electrons is given by

$$U_{cr} = m_e c^2 \int_{\gamma_0}^{\gamma_*} n(\gamma) \gamma d\gamma = m_e c^2 n_0 \frac{\gamma_*^{2-p}}{2-p}. \quad (4)$$

where we assumed that the spectrum is sufficiently hard,  $p < 2$ , which is consistent with acceleration in shocks or sites of magnetic reconnection. It is reasonable to assume that this energy is comparable to the thermal or rms energy of the plasma motion, e.g.,  $U_{cr} \sim 10^3$  eV/cm<sup>3</sup>.

The average power radiated by an ultra-relativistic electron is

$$\langle P \rangle = \frac{4}{3} \sigma_T c \gamma^2 \frac{B^2}{8\pi}, \quad (5)$$

where  $\sigma_T \approx 6.65 \times 10^{-25} \text{cm}^2$  is the Thompson cross section. Therefore, the total radiated power is:

$$L_s = \int_{\gamma_0}^{\gamma_*} \langle P \rangle n(\gamma) d\gamma = \frac{4}{3} \sigma_T c \frac{B^2}{8\pi} \int_{\gamma_0}^{\gamma_*} n(\gamma) \gamma^2 d\gamma = \frac{4}{3} \sigma_T c \frac{B^2}{8\pi} n_0 \frac{\gamma_*^{3-p}}{3-p}. \quad (6)$$

and the characteristic cooling rate of the electrons is estimated as:

$$\frac{1}{\tau} \approx \frac{L_s}{U_{cr}} = \frac{\frac{4}{3} \sigma_T c}{m_e c^2} \frac{B^2}{8\pi} \left( \frac{2-p}{3-p} \right) \gamma_*. \quad (7)$$

For  $B = 0.1 \text{ mG}$ , the cooling time is

$$\tau \approx 2.5 \times 10^9 \left( \frac{3-p}{2-p} \right) \frac{1}{\gamma_*} \text{ years}. \quad (8)$$

So, if the electrons can be accelerated to large energies  $\gamma_* m_e c^2 \sim \text{TeV}$ , the cooling time may be quite short. For instance, for  $p = 1.5$  and  $\gamma_* = 10^7$ , we estimate  $\tau \approx 750$  years.

A short cooling time of the plasma can trigger the cooling instability, whose growth rate is comparable to the cooling rate. Indeed, as plasma gets compressed, the magnetic strength increases while the transverse scale of the compressed region,  $l$ , decreases. The typical time of nonlinear evolution of the compressed plasma structure is  $t_{nl} \sim l/v$ , where the speed of plasma flow in the developing structure is comparable to the speed of sound,  $v \sim v_s$ . One can estimate  $v_s \sim 500 \text{ km/s}$  for typical plasma density in the central 150 pc and energy density of  $10^3 \text{ eV/cm}^3$ . Equating the nonlinear time to the cooling time and assuming  $\gamma_* \sim 10^7$ , we estimate the transverse size of the plasma region where the cooling instability sets in as  $l \leq \pi \tau v_s \sim 3 \times 10^{18} \text{ cm}$ , which is consistent with observations.

The cooling instability further compresses magnetic field lines and may split a magnetic filament into sub-filaments separated from each other in the transverse direction. Indeed, for transverse wave numbers  $k > 1/(\tau v_s)$ , the cooling instability growth rate is virtually independent of the wave number, and therefore, even thinner sub-filaments may, in principle, be formed. One, however, may argue that the compressed region still possesses plasma turbulence. Nonlinear evolution rates in turbulence are typically higher at smaller scales, therefore, the thinner substructures would have nonlinear interaction rates exceeding  $1/\tau$ , while the instability rate is still  $1/\tau$ . Therefore, the development of the instability would be impeded by turbulent disruption at smaller scales. It is, therefore, reasonable to assume that the typical space between sub-filaments should be comparable to the thickness of a filament region itself,  $\Delta l \sim l \sim v_s \tau$ , that is, only a few sub-filaments should be expected in each filamentary structure.

Another possible filament forming mechanism that does not require rapid cooling involves an active turbulent medium. In this picture, turbulent compression of the magnetic field in the cosmic-ray driven nuclear wind, can explain the synchrotron emissivity. Such compressed field regions could arise as a result of active turbulent medium (Boldyrev & Yusef-Zadeh 2006). In the turbulent picture, the spatial distribution of the magnetic field energy is highly intermittent, and the regions of strong field have filamentary structure. Finally, a recent study of filament groupings that exhibit sorting by filament length suggested that the synchrotron-emitting electrons are produced by a time-dependent injecting source or crossing spatially intermittent magnetic bundles (Thomas, Pfrommer, & Enßlin 2020). While this model may be applicable to some systems, many examples do not exhibit this ordering in their filament lengths and there are no obvious compact sources running across them.

#### 4.4. Summary

We have concentrated on morphological and spectral studies of some of the most spectacular groupings of filaments in the Galactic center. The filaments run parallel to each other, shift sideways together or converge to a point suggesting that the filaments in a grouping are physically associated with each other rather than being chance line-of-sight associations. Furthermore, the morphology of individual grouping suggests that the magnetic field of the filaments change direction coherently implying that they are parts of a large-scale magnetic structure. We determined a new characteristic of the population of the filaments in a grouping in that they are spaced from each other with the mean value of  $\sim 16''$ . We also determined the mean width span of all filament groupings is  $\sim 27''$ . We modeled and reproduced the observed distribution of filament spacing assuming that the filament groupings are randomly oriented with respect to the line of sight. This assumes that the Galactic center filaments are one-dimensional and are not limb-brightened sheet-like structures viewed edge-on.

We note a number of striking examples of two-pronged forked filaments with a compact source detected at the junction. The spectral index variation along the length of the filaments and morphological changes such as the width, curvature and brightness support the scenario of a flow of thermal plasma being carried along the length of the filaments. Another striking result is the spectral index variation of harp-like filaments, where there is a tendency for filaments with the longest lengths to have steeper spectra. This correlation between length and spectral index variation implies that cosmic ray particles in short filaments are more recently accelerated than longer filaments.

As for the cause of filamentation observed throughout the Galactic center, we explored a new possibility that filamentation occurs because of synchrotron cooling instability. Rapid synchrotron cooling can trigger the instability and forming sub-filaments parallel to each other with a spacing that is similar scale to observed values of  $\sim 0.5 - 1$  pc. Another possibility is that filamentation is triggered as a result of a large-scale, cosmic-ray driven nuclear wind with an obstacle. In this picture, the obstacle, which could be stellar wind bubble, an HII region or a cloud, compresses the magnetic field and forms a filament in the direction opposite to the motion of the obstacle with respect to the direction of the nuclear wind. Thus, the structure of the obstacle is imprinted on the number of parallel filaments. Future high-resolution observations will test the obstacle picture.

## 5. DATA AVAILABILITY

All the data including VLA and MeerKAT that we used here are available online and are not proprietary. We have reduced and calibrated these data and are available if requested.

## 6. ACKNOWLEDGMENTS

Work by R.G.A. was supported by NASA under award number 80GSFC21M0002. FYZ is partially supported by the grant AST-0807400 from the the National Science Foundation. The MeerKAT telescope is operated by the South African Radio Astronomy Observatory, which is a facility of the National Research Foundation, an agency of the Department of Science and Innovation. The authors acknowledge the Center for High Performance Computing (CHPC), South Africa, for providing computational resources to this research project. The National Radio Astronomy Observatory is a facility of the National Science Foundation operated under cooperative agreement by Associated Universities, Inc. IH acknowledges support from the UK Science and Technology Facilities Council [ST/N000919/1], and from the South African Radio Astronomy Observatory which is a facility of the National Research Foundation (NRF), an agency of the Department of Science and Innovation. The work of SB was partly supported by NSF Grant PHY-2010098, by NASA Grant 80NSSC18K0646, and by the Wisconsin Plasma Physics Laboratory (US Department of Energy Grant DE-SC0018266).

*Facilities:* VLA, MeerKAT

## REFERENCES

- Anantharamaiah K. R., Pedlar A., Ekers R. D., Goss W. M., 1991, MNRAS, 249, 262.  
doi:10.1093/mnras/249.2.262
- Anantharamaiah K. R., Lang C. C., Kassim N. E., Lazio T. J. W., Goss W. M., 1999, ASPC, 186, 507
- Arendt R. G., Staguhn J., Dwek E., Morris M. R., Yusef-Zadeh F., Benford D. J., Kovács A., et al., 2019, ApJ, 885, 71. doi:10.3847/1538-4357/ab451c
- Aschwanden M. J., 2010, SoPh, 262, 399
- Bally J., Yusef-Zadeh F., 1989, ApJ, 336, 173.  
doi:10.1086/167003
- Banda-Barragán W. E., Parkin E. R., Federrath C., Crocker R. M., Bicknell G. V., 2016, MNRAS, 455, 1309
- Bicknell G. V., Li J., 2001, ApJ, 548, L69
- Boldyrev S., Yusef-Zadeh F., 2006, ApJL, 637, L101.  
doi:10.1086/500411
- Chuard D., Terrier R., Goldwurm A., Clavel M., Soldi S., Morris M. R., Ponti G., et al., 2018, A&A, 610, A34.  
doi:10.1051/0004-6361/201731864
- Coughlin E. R., Nixon C. J., Ginsburg A., 2021, MNRAS, 501, 1868. doi:10.1093/mnras/staa3771
- Dahlburg R. B., Einaudi G., LaRosa T. N., Shore S. N., 2002, ApJ, 568, 220
- Drake J. F., Swisdak M., Fermo R., 2013, ApJL, 763, L5.  
doi:10.1088/2041-8205/763/1/L5
- Ferrière K., 2009, A&A, 505, 1183
- Geballe T. R., McCall B. J., Hinkle K. H., Oka T., 1999, ApJ, 510, 251
- Goto M., Geballe T. R., Indriolo N., Yusef-Zadeh F., Usuda T., Henning T., Oka T., 2014, ApJ, 786, 96
- Gray A. D., Cram L. E., Ekers R. D., Goss W. M., 1991, Natur, 353, 237

- Gray A. D., Nicholls J., Ekers R. D., Cram L. E., 1995, *ApJ*, 448, 164
- Green D. A., 1988, *Ap&SS*, 148, 3. doi:10.1007/BF00646462
- Guo F., Liu Y.-H., Li X., Li H., Daughton W., Kilian P., 2020, *PhPl*, 27, 080501. doi:10.1063/5.0012094
- Haynes R. F., Stewart R. T., Gray A. D., Reich W., Reich P., Mebold U., 1992, *A&A*, 264, 500
- Henshaw J. D., Barnes A. T., Battersby C., Ginsburg A., Sormani M. C., Walker D. L., 2022, arXiv, arXiv:2203.11223
- Heywood I. et al. 2019, *Nature*, 10.1038
- Heywood I., Rammala I., Camilo F., Cotton W. D., Yusef-Zadeh F., Abbott T. D., Adam R. M., et al., 2022, *ApJ*, 925, 165. doi:10.3847/1538-4357/ac449a
- Heywood I., Rammala I., Camilo F., Cotton W. D., Yusef-Zadeh F., Abbott T. D., Adam R. M., et al., 2022, *ApJ*, 925, 165. doi:10.3847/1538-4357/ac449a
- Indriolo N., McCall B. J., 2012, *ApJ*, 745, 91
- Inoue M., Takahashi T., Tabara H., Kato T., Tsuboi M., 1984, *PASJ*, 36, 633
- Johnson S. P., Dong H., Wang Q. D., 2009, *MNRAS*, 399, 1429
- Kassim N. E., Frail D. A., 1996, *MNRAS*, 283, L51. doi:10.1093/mnras/283.3.L51
- Lang C. C., Anantharamaiah K. R., Kassim N. E., Lazio T. J. W., 1999, *ApJL*, 521, L41. doi:10.1086/312180
- Lang C. C., Morris M., Echevarria L., 1999, *ApJ*, 526, 727
- LaRosa T. N., Lazio T. J. W., Kassim N. E., 2001, *ApJ*, 563, 163
- LaRosa T. N., Nord M. E., Lazio T. J. W., Kassim N. E., 2004, *ApJ*, 607, 302
- Law C. J., Yusef-Zadeh F., Cotton W. D., 2008, *ApJS*, 177, 515
- Le Petit, F., Ruaud, M., Bron, E., et al. 2016, *A&A*, 585, A105
- Liszt H. S., 1985, *ApJ*, 293, L65
- Lu F. J., Wang Q. D., Lang C. C., 2003, *AJ*, 126, 319
- Lu F. J., Yuan T. T., Lou Y.-Q., 2008, *ApJ*, 673, 915
- Martinez K. M., 2020, PhDT
- Morris, M. 2006, *Journal of Physics Conference Series*, 54, 1. doi:10.1088/1742-6596/54/1/001
- Morris, M. 2007, astro-ph/0701050
- Muno M. P., Baganoff F. K., Brandt W. N., Morris M. R., Starck J.-L., 2008, *ApJ*, 673, 251
- Nord M. E., Lazio T. J. W., Kassim N. E., Hyman S. D., LaRosa T. N., Brogan C. L., Duric N., 2004, *AJ*, 128, 1646.
- Nicholls J., Le Strange E. T., 1995, *ApJ*, 443, 638
- Oka T., Geballe T. R., Goto M., Usuda T., McCall B. J., 2005, *ApJ*, 632, 882
- Oka T., Geballe T. R., Goto M., Usuda T., McCall B. J., 2019, *ApJ*, in press
- Paré D. M., Lang C. C., Morris M. R., Moore H., Mao S. A., 2019, *ApJ*, 884, 170. doi:10.3847/1538-4357/ab45ed
- Ponti, G., Hofmann, F., Churazov, E., et al. 2019, *Nature*, 567, 347
- Ponti G., Morris M. R., Terrier R., Haberl F., Sturm R., Clavel M., Soldi S., et al., 2015, *MNRAS*, 453, 172. doi:10.1093/mnras/stv1331
- Pound M. W., Yusef-Zadeh F., 2018, *MNRAS*, 473, 2899. doi:10.1093/mnras/stx2490
- Royster M. J., Hewitt J. W., Roberts D. A., Yusef-Zadeh F., 2011, *ASPC*, 439, 31
- Rosner R., Bodo G., 1996, *ApJ*, 470, L49
- Sakano M., Warwick R. S., Decourchelle A., Predehl P., 2003, *MNRAS*, 340, 747
- Schuller F., Urquhart J. S., Csengeri T., Colombo D., Duarte-Cabral A., Mattern M., Ginsburg A., et al., 2021, *MNRAS*, 500, 3064. doi:10.1093/mnras/staa2369
- Simon M., Axford W. I., 1967, *ApJ*, 150, 105. doi:10.1086/149316
- Shore S. N., LaRosa T. N., 1999, *ApJ*, 521, 587
- Staguhn J., Arendt R. G., Dwek E., Morris M. R., Yusef-Zadeh F., Benford D. J., Kovács A., et al., 2019, *ApJ*, 885, 72. doi:10.3847/1538-4357/ab451b
- Staguhn J., Stutzki J., Uchida K. I., Yusef-Zadeh F., 1998, *A&A*, 336, 290
- Sofue Y., Handa T., 1984, *Natur*, 310, 568
- Sofue Y., 2020, *PASJ*, 72, L4. doi:10.1093/pasj/psaa011
- Su, M., Slatyer, T. R., & Finkbeiner, D. P. 2010, *ApJ*, 724, 1044
- Staguhn J., Stutzki J., Uchida K. I., Yusef-Zadeh F., 1998, *A&A*, 336, 290
- Thomas T., Pfrommer C., Enßlin T., 2020, *ApJL*, 890, L18. doi:10.3847/2041-8213/ab7237
- Tsuboi M., Kawabata T., Kasuga T., Handa T., Kato T., 1995, *PASJ*, 47, 829
- Wang Q. D., Lu F., Lang C. C., 2002, *ApJ*, 581, 1148.
- Yusef-Zadeh F., Bally J., 1987, *Natur*, 330, 455. doi:10.1038/330455a0
- Yusef-Zadeh F., Morris M., 1988, *ApJ*, 329, 729. doi:10.1086/166417
- Yusef-Zadeh F., Wardle M., Heinke C., Heywood I., Arendt R., Royster M., Cotton W., et al., 2021, *MNRAS*, 500, 3142. doi:10.1093/mnras/staa3257
- Yusef-Zadeh, F. 2003, *ApJ*, 598, 325.
- Yusef-Zadeh F., Muno M., Wardle M., Lis D. C., 2007, *ApJ*, 656, 847. doi:10.1086/510663

- Yusef-Zadeh F., Wardle M., Heinke C., Heywood I., Arendt R., Royster M., Cotton W., et al., 2021, MNRAS, 500, 3142. doi:10.1093/mnras/staa3257
- Yusef-Zadeh F., Wardle M., 2019, MNRAS, 490, L1
- Yusef-Zadeh F., Morris M., Chance D., 1984, Natur, 310, 557
- Yusef-Zadeh F., Arendt R. G., Wardle M., Heywood I., Cotton W., Camilo F., 2022, ApJL, 925, L18. doi:10.3847/2041-8213/ac4802
- Yusef-Zadeh F., Wardle M., Heinke C., Heywood I., Arendt R., Royster M., Cotton W., et al., 2021, MNRAS, 500, 3142. doi:10.1093/mnras/staa3257
- Yusef-Zadeh F., Wardle M., Parastaran P., 1997, ApJ, 475, L119
- Yusef-Zadeh, F., Hewitt, J. W., & Cotton, W. 2004, ApJS, 155, 421.
- Yusef-Zadeh F., Munoz M., Wardle M., Lis D. C., 2007, ApJ, 656, 847
- Yusef-Zadeh F., Wardle M., Roy S., 2007, ApJ, 665, L123
- Yusef-Zadeh F., et al., 2013, ApJ, 762, 33
- Yusef-Zadeh F., Wardle M., Munoz M., Law C., Pound M., 2005, AdSpR, 35, 1074
- Yusef-Zadeh F., Wardle M., 2019, MNRAS, 490, L1
- Yusef-Zadeh F., Morris M., Slee O. B., Nelson G. J., 1986, ApJ, 310, 689. doi:10.1086/164719
- Yusef-Zadeh F., Morris M., 1987, ApJ, 322, 721. doi:10.1086/165767
- Yusef-Zadeh F., 2003, ApJ, 598, 325. doi:10.1086/378715
- Zhang S., et al., 2014, ApJ, 784, 6
- Zhang S., et al., 2020, ApJ, 893, 3

## APPENDIX

## A. APPENDIX

To examine projection effects on the filament spacings, consider a pair of filaments with perpendicular separation  $h_0$ , represented by the lines  $(x, h_0, 0)$  and  $(x, 0, 0)$  in a Cartesian coordinate system  $(x, y, z)$ . Suppose that the direction to the observer is  $(\phi, \theta)$  in the associated spherical polar coordinates. To find the apparent separation of the lines as projected in the plane of the observer's sky, we construct another coordinate system  $(x', y', z')$  having the same origin, with the  $z'$ -axis directed to the observer so that the sky-plane coordinates are  $(x', y')$ . We may choose the  $y'$ -axis to be parallel to the projection of the  $y$ -axis on the plane of the observer's sky; then the coordinate systems are related by the transformation

$$\begin{pmatrix} x' \\ y' \\ z' \end{pmatrix} = \begin{pmatrix} \cos \theta \cos \phi & \cos \theta \sin \phi & \sin \theta \\ -\sin \phi & \cos \phi & 0 \\ \sin \theta \cos \phi & \sin \theta \sin \phi & \cos \theta \end{pmatrix} \begin{pmatrix} x \\ y \\ z \end{pmatrix}. \quad (\text{A1})$$

The coordinates tracing the filaments in the observer's sky are

$$x' = \cos \theta (x \cos \phi + a \sin \phi) \quad (\text{A2})$$

$$y' = -x \sin \phi + a \cos \phi \quad (\text{A3})$$

i.e.

$$y' = -x' \tan \phi \sec \theta + a \sec \phi \quad (\text{A4})$$

with  $a = 0$  and  $h_0$ . Then the apparent plane-of-sky distance between the two filaments is

$$h = \frac{h_0}{\sqrt{1 + \sin^2 \phi \tan^2 \theta}}. \quad (\text{A5})$$

Assuming that the filament systems are randomly oriented, the joint probability distribution of the observer's viewing angles is

$$P(\phi, \theta) = \frac{\sin \theta}{4\pi}, \quad (\text{A6})$$

which we convert to a joint probability density in  $(\phi, h)$ :

$$P(\phi, h) = P(\phi, \theta) \left| \frac{\partial h}{\partial \theta} \right|^{-1} = \frac{2}{\pi} \frac{|\sin \phi|}{\sqrt{h_0^2 - h^2 \cos^2 \phi}}, \quad (\text{A7})$$

and then integrate over  $\phi$  to obtain the probability density  $h$  given  $h_0$ , given in equation (1).

**Table 1.** The mean angular separation of filaments in groups

| Group<br>Number | Group<br>Name  | $l$<br>(deg) | $b$<br>(deg) | Span<br>(asec) | Number of<br>filaments | Mean Separation<br>(asec) | Figure<br>Number |
|-----------------|----------------|--------------|--------------|----------------|------------------------|---------------------------|------------------|
| 0               | Horseshoe      | 358.743      | -0.215       | 18.0           | 2                      | 18.0                      | 2                |
| 1               | Pelican        | 358.828      | 0.471        | 45.1           | 4                      | 15.0                      | 3                |
| 2               | Arrow          | 359.128      | 0.634        | 45.1           | 2                      | 45.1                      | 4                |
| 3               | Snake-1        | 359.132      | -0.296       | 33.2           | 2                      | 33.2                      | 5                |
| 4               | Snake-2        | 359.159      | -0.111       | 28.8           | 3                      | 14.4                      | 5                |
| 5               | Snake-3        | 359.196      | -0.474       | 131.8          | 5                      | 33.0                      | 5                |
| 6               | Candle         | 359.221      | -0.129       | 25.2           | 4                      | 8.4                       | 6                |
| 7               | Hummingbird-1  | 359.300      | -0.175       | 15.6           | 2                      | 15.6                      | 8                |
| 8               | Sausage        | 359.317      | -0.430       | 21.0           | 2                      | 21.0                      | 7                |
| 9               | Hummingbird-2  | 359.366      | -0.140       | 82.1           | 5                      | 20.5                      | 8                |
| 10              | River          | 359.397      | -0.187       | 21.6           | 2                      | 21.6                      | 12               |
| 11              | Forceps        | 359.399      | -0.213       | 18.0           | 2                      | 18.0                      | 12               |
| 12              | Feather        | 359.411      | -0.709       | 35.5           | 3                      | 17.7                      | 9                |
| 13              | Sgr C-1        | 359.425      | 0.043        | 41.0           | 3                      | 20.5                      | 10               |
| 14              | French Knife   | 359.429      | 0.132        | 21.4           | 3                      | 10.7                      | 11               |
| 15              | Sgr C-2        | 359.446      | -0.005       | 25.8           | 2                      | 25.8                      | 10               |
| 16              | Bent Harp      | 359.484      | 0.122        | 53.1           | 5                      | 13.3                      | 13               |
| 17              | Concorde       | 359.495      | 0.188        | 26.2           | 3                      | 13.1                      | 11               |
| 18              | Cataract       | 359.504      | -0.321       | 289.8          | 8                      | 41.4                      | 12               |
| 19              | Ripple         | 359.520      | 0.237        | 36.0           | 3                      | 18.0                      | 14               |
| 20              | Edge-on Spiral | 359.563      | 0.249        | 28.1           | 2                      | 28.1                      | 14               |
| 21              | Broken Harp-1  | 359.625      | 0.298        | 31.8           | 4                      | 10.6                      | 15               |
| 22              | Broken Harp-2  | 359.640      | 0.308        | 77.4           | 6                      | 15.5                      | 15               |
| 23              | Waterfall      | 359.687      | -0.435       | 90.0           | 6                      | 18.0                      | 16               |
| 24              | Hilltop        | 359.702      | -0.517       | 29.7           | 5                      | 7.4                       | 16               |
| 25              | Flamingo-1     | 359.717      | 0.228        | 33.2           | 3                      | 16.6                      | 18               |
| 26              | Knot           | 359.738      | -0.792       | 21.0           | 2                      | 21.0                      | 17               |
| 27              | Flamingo-2     | 359.808      | 0.130        | 32.4           | 3                      | 16.2                      | 18               |
| 28              | Eyebrow        | 359.830      | 0.085        | 29.2           | 3                      | 14.6                      | 18               |
| 29              | Harp           | 359.851      | 0.374        | 91.5           | 8                      | 13.1                      | 20               |
| 30              | Cleaver        | 359.890      | -0.289       | 23.1           | 2                      | 23.1                      | 19               |
| 31              | Comet Tail     | 359.992      | -0.572       | 54.9           | 3                      | 27.5                      | 21               |
| 32              | Radio Arc S-1  | 0.138        | -0.299       | 249.3          | 12                     | 22.7                      | 22               |
| 33              | Radio Arc      | 0.160        | -0.115       | 224.5          | 17                     | 14.0                      | 23               |
| 34              | Ring           | 0.168        | 0.142        | 96.9           | 7                      | 16.2                      | 24               |
| 35              | Radio Arc S-2  | 0.172        | -0.423       | 18.4           | 2                      | 18.4                      | 22               |
| 36              | Space Shuttle  | 0.228        | 0.812        | 29.0           | 3                      | 14.5                      | 25               |
| 37              | Porcupine-1    | 0.288        | -0.259       | 20.3           | 4                      | 6.8                       | 26               |
| 38              | Porcupine-2    | 0.297        | -0.266       | 62.8           | 7                      | 10.5                      | 26               |
| 39              | Porcupine-3    | 0.306        | -0.273       | 28.6           | 3                      | 14.3                      | 26               |
| 40              | Contrail       | 0.405        | -0.277       | 31.0           | 3                      | 15.5                      | 27               |
| 41              | Bent Fork      | 0.687        | 0.147        | 7.5            | 2                      | 7.5                       | 28               |
| 42              | Meteor Trail   | 0.859        | -0.597       | 25.5           | 2                      | 25.5                      | 29               |
| Robust mean     |                |              |              | 27±8           |                        | 16±7                      |                  |

**Table 2.** Compact sources and locations of interest

| Name           | $l$ (deg) | $b$ (deg) | Type     | Figure |
|----------------|-----------|-----------|----------|--------|
| G358.693-0.227 | 358.693   | -0.227    | Source   | 2      |
| G358.733-0.229 | 358.733   | -0.229    | Source   | 2      |
| G358.776+0.454 | 358.776   | 0.454     | Source   | 3      |
| G358.794+0.479 | 358.794   | 0.479     | Source   | 3      |
| G358.798+0.468 | 358.798   | 0.468     | Source   | 3      |
| G359.072+0.735 | 359.072   | 0.735     | Source   | 4      |
| G359.120-0.265 | 359.120   | -0.265    | Source   | 5      |
| G359.132-0.200 | 359.132   | -0.200    | Source   | 5      |
| G359.211-0.085 | 359.211   | -0.085    | Source   | 6      |
| G359.214-0.100 | 359.214   | -0.100    | Source   | 6      |
| G359.224-0.136 | 359.224   | -0.136    | Source   | 6      |
| G359.321-0.158 | 359.321   | -0.158    | Location | 8      |
| G359.321-0.431 | 359.321   | -0.431    | Source   | 7      |
| G359.324-0.430 | 359.324   | -0.430    | Source   | 7      |
| G359.344-0.416 | 359.344   | -0.416    | Source   | 7      |
| G359.401-0.238 | 359.401   | -0.238    | Location | 12     |
| G359.405-0.259 | 359.405   | -0.259    | Location | 12     |
| G359.416-0.706 | 359.416   | -0.706    | Source   | 9      |
| G359.419-0.583 | 359.419   | -0.583    | Source   | 9      |
| G359.420-0.660 | 359.420   | -0.660    | Location | 9      |
| G359.423-0.664 | 359.423   | -0.664    | Source   | 9      |
| G359.439+0.006 | 359.439   | 0.006     | Location | 10     |
| G359.439+0.103 | 359.439   | 0.103     | Location | 11     |
| G359.453-0.033 | 359.453   | -0.033    | Location | 10     |
| G359.455-0.055 | 359.455   | -0.055    | Source   | 10     |
| G359.467-0.171 | 359.467   | -0.171    | Source   | 12     |
| G359.475+0.127 | 359.475   | 0.127     | Source   | 13     |
| G359.485+0.121 | 359.485   | 0.121     | Source   | 13     |
| G359.491+0.121 | 359.491   | 0.121     | Source   | 13     |
| G359.522+0.097 | 359.522   | 0.097     | Source   | 13     |
| G359.557+0.140 | 359.557   | 0.140     | Source   | 14     |
| G359.729-0.811 | 359.729   | -0.811    | Location | 17     |
| G359.734-0.801 | 359.734   | -0.801    | Location | 17     |
| G359.746-0.784 | 359.746   | -0.784    | Source   | 17     |
| G359.748-0.781 | 359.748   | -0.781    | Source   | 17     |
| G359.758+0.198 | 359.758   | 0.198     | Location | 18     |
| G359.808+0.117 | 359.808   | 0.117     | Source   | 18     |
| G359.838+0.375 | 359.838   | 0.375     | Source   | 20     |
| G359.841+0.366 | 359.841   | 0.366     | Source   | 20     |
| G359.844+0.358 | 359.844   | 0.358     | Source   | 20     |
| G359.848+0.298 | 359.848   | 0.298     | Source   | 20     |
| G359.851+0.293 | 359.851   | 0.293     | Source   | 20     |
| G359.874-0.264 | 359.874   | -0.264    | Source   | 19     |
| G359.886+0.102 | 359.886   | 0.102     | Source   | 18     |
| G359.921-0.283 | 359.921   | -0.283    | Location | 19     |
| G359.950-0.259 | 359.950   | -0.259    | Source   | 19     |
| G359.992-0.555 | 359.992   | -0.555    | Location | 21     |
| G0.023-0.626   | 0.023     | -0.626    | Location | 21     |
| G0.030-0.660   | 0.030     | -0.660    | Source   | 21     |
| G0.034-0.661   | 0.034     | -0.661    | Source   | 21     |
| G0.045-0.668   | 0.045     | -0.668    | Source   | 21     |
| G0.225+0.843   | 0.225     | 0.843     | Source   | 25     |
| G0.226+0.792   | 0.226     | 0.792     | Source   | 25     |
| G0.264-0.197   | 0.264     | -0.197    | Source   | 26     |
| G0.420-0.297   | 0.420     | -0.297    | Location | 27     |
| G0.421-0.290   | 0.421     | -0.290    | Location | 27     |
| G0.443-0.324   | 0.443     | -0.324    | Location | 27     |
| G0.697+0.148   | 0.697     | 0.148     | Source   | 28     |

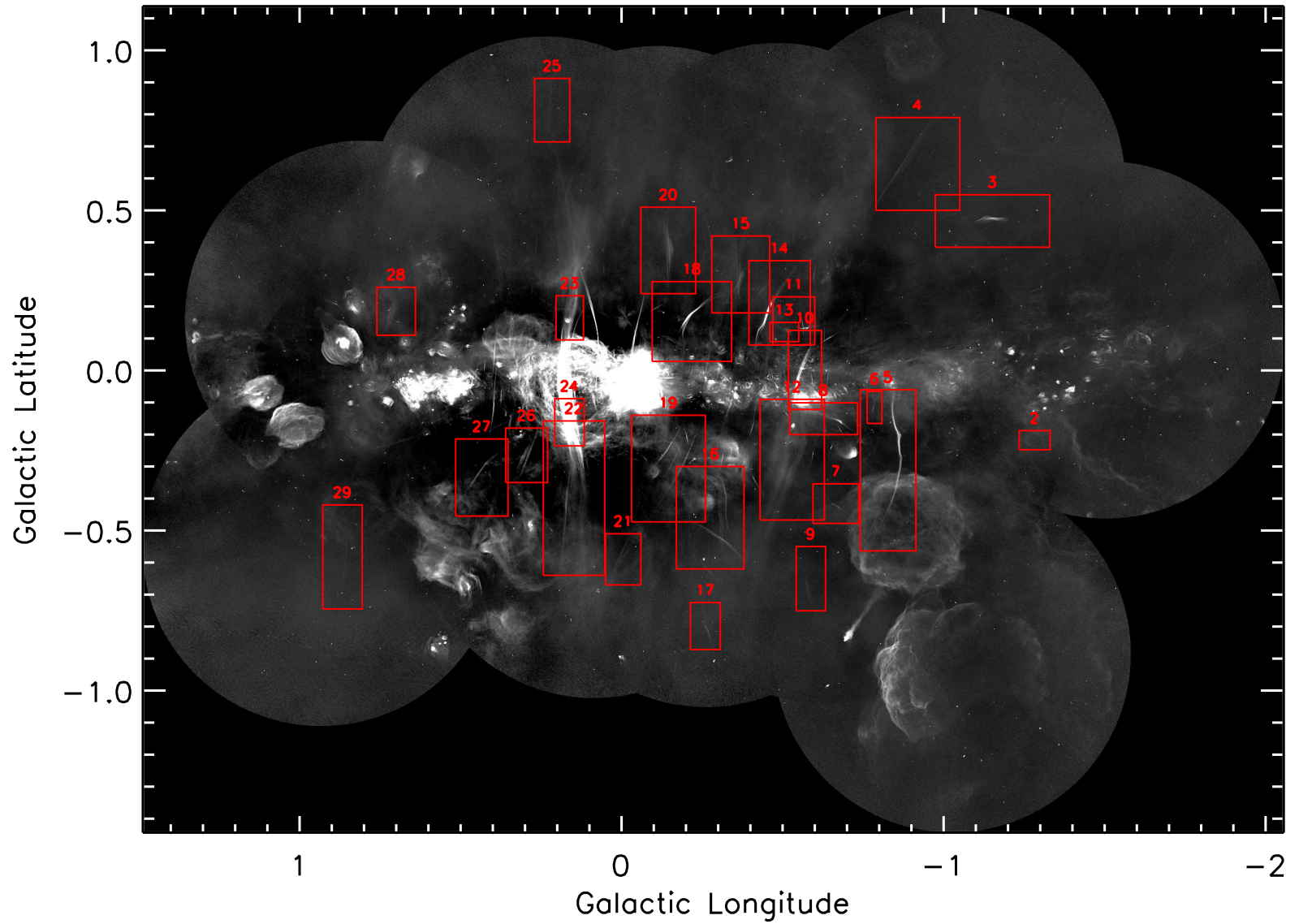


**Figure 1.** A 1.28 GHz mosaic image of the Galactic center region (Heywood et al. 2022). Red boxes show groupings that are described here. There are 27 boxes corresponding to the number of figures between 2 and 28.

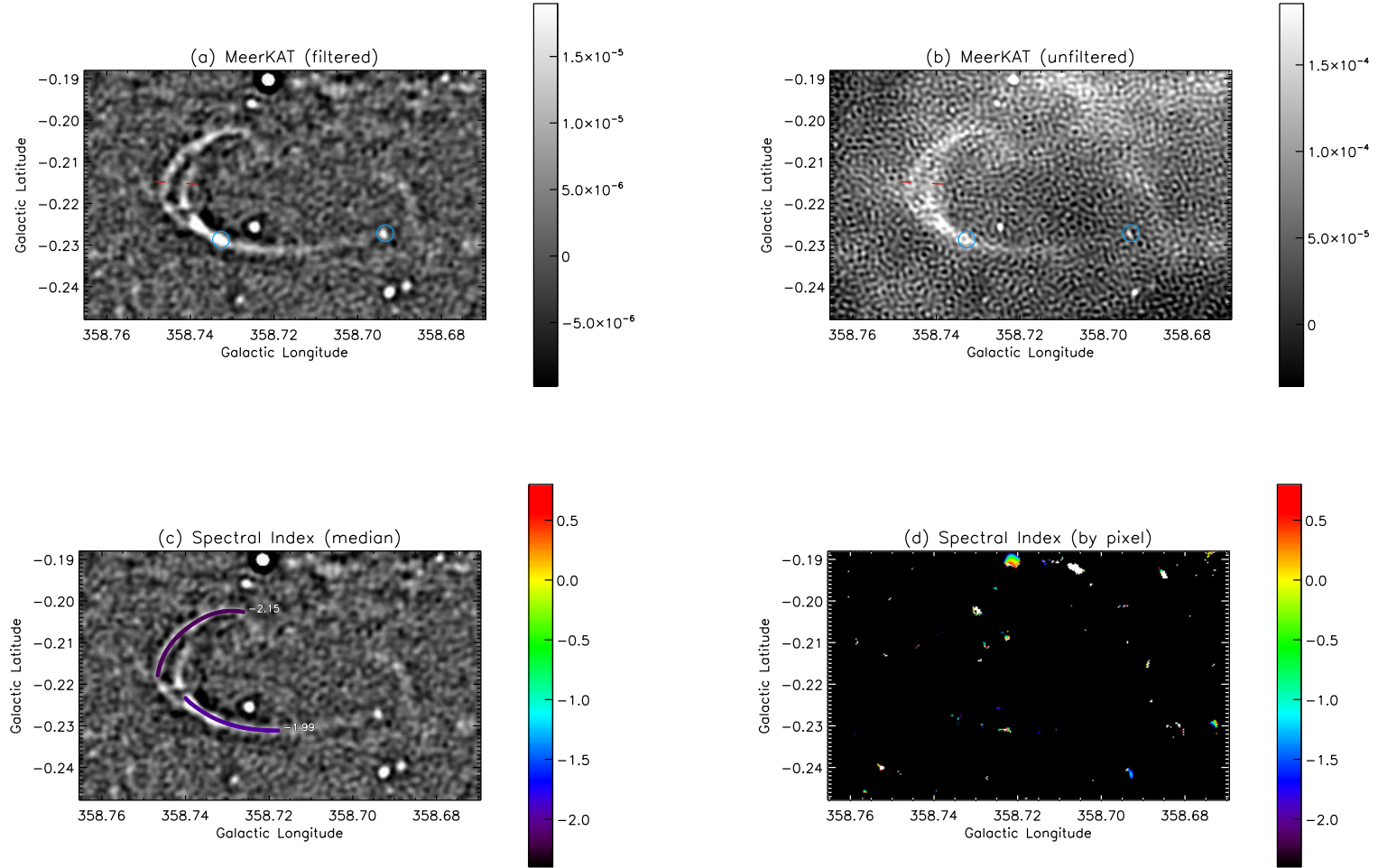


**Figure 2.** (The Horseshoe) Filtered (a) and unfiltered (b) 1.28 GHz continuum images of a horseshoe-shaped grouping G358.743-0.215 are shown in the top two panels. Mean (c) and pixel-by-pixel (d) spectral indices of the filaments are displayed in the bottom two panels. The red markings seen as two short line segments in unfiltered images indicate where the filament spacing was measured, as listed in Table 1. The tabulated coordinates are where the center of the marking lies. Blue and red circles represent point (or compact) sources and general locations of interest, respectively. The scale bars with the filtered and unfiltered images show the intensity grayscale Jy per  $4'' \times 4''$  beam. The intensity of the filtered image does not account for changes in beam which is roughly a filtering factor of 7.1. The color scale bars show spectral index values in panels (c) and (d). As a more precise guide, the median spectral index value is printed at one end of each detected filament in panel (c). “NaN” values indicate filaments that are detected in intensity but are too faint to have reliable spectral indices.

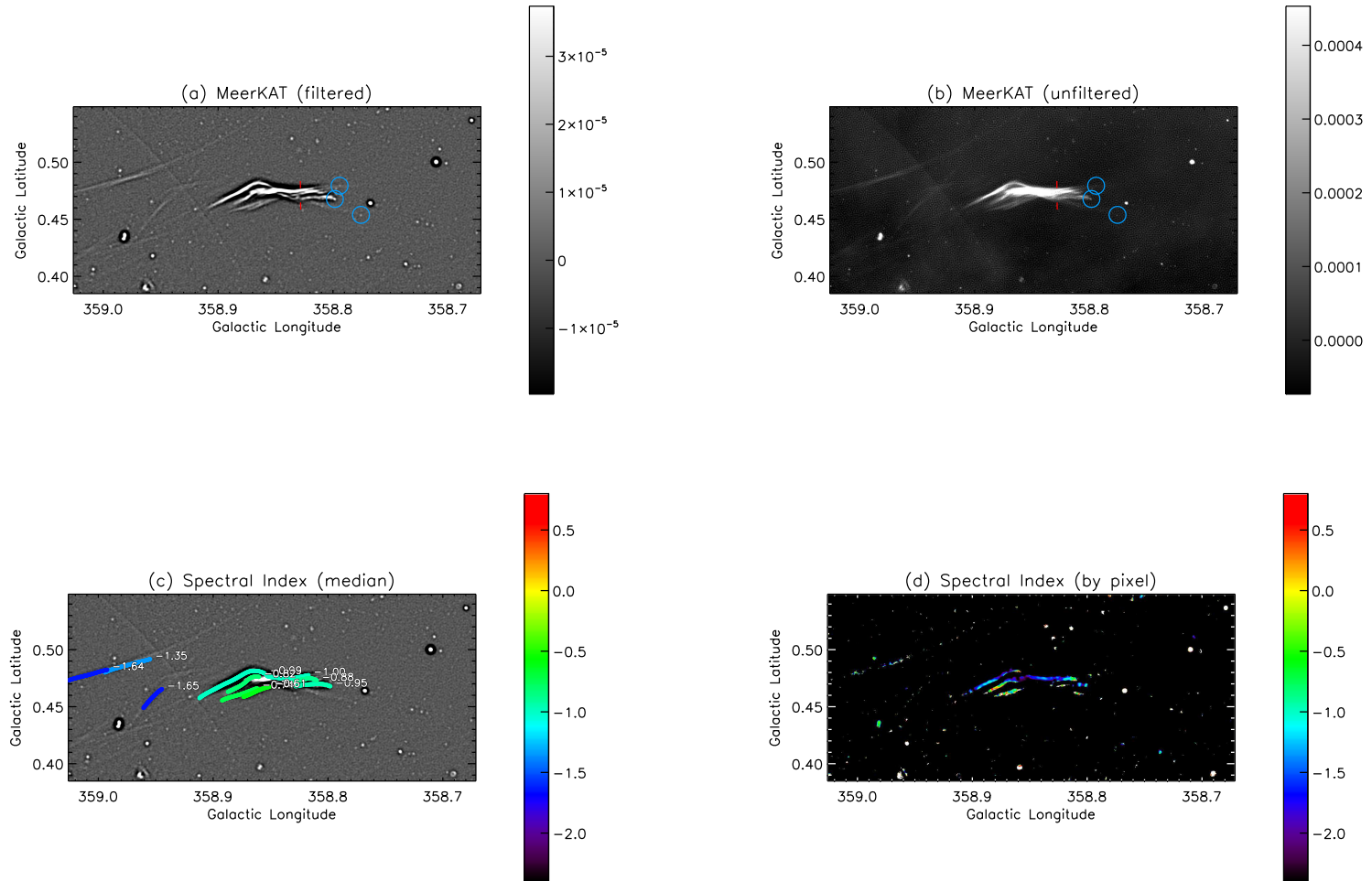


**Figure 3.** (The Pelican) Same as Figure 2 except G358.828+0.471 filaments are displayed.

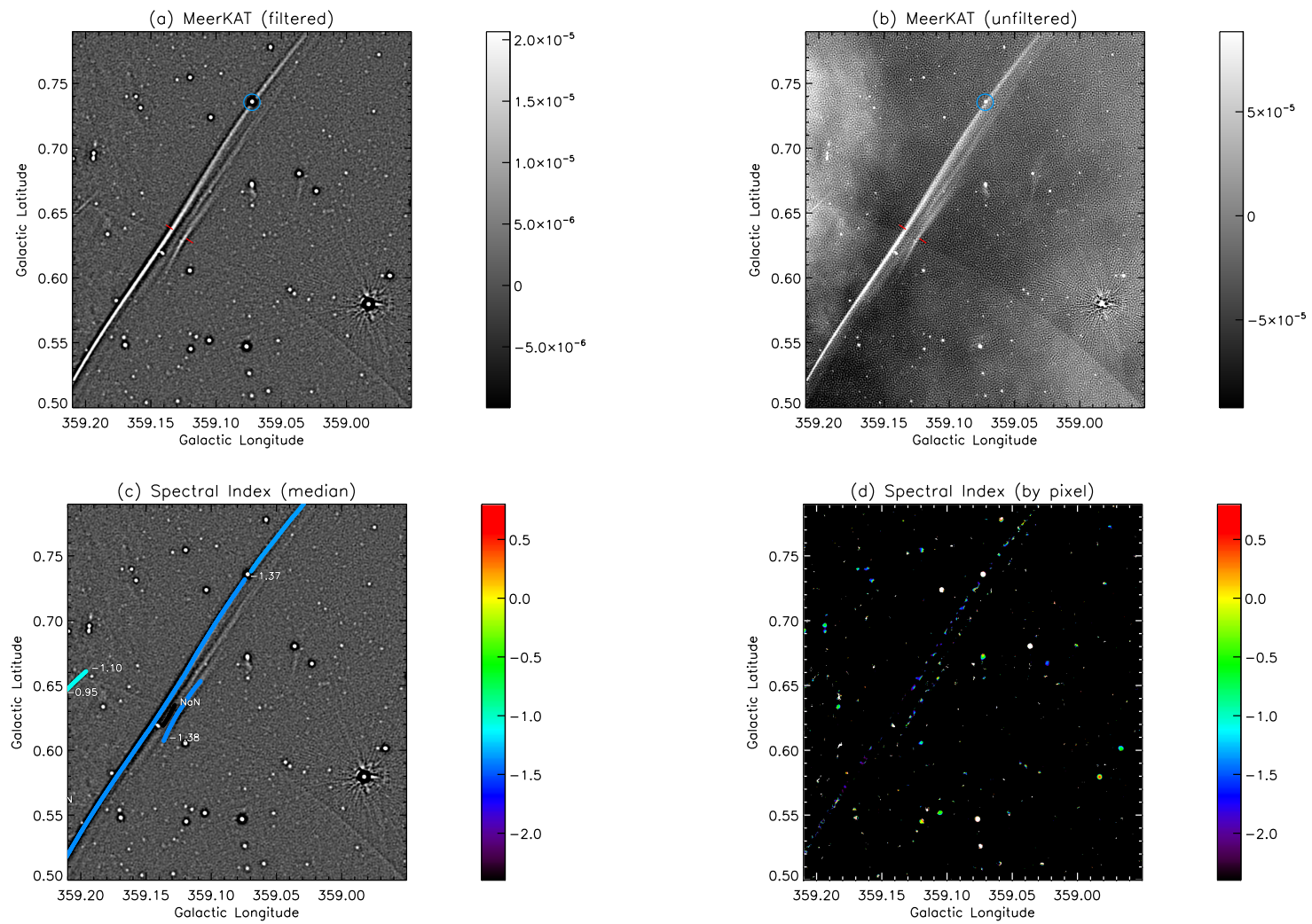


**Figure 4.** (The Arrow) Same as Figure 2 except that G359.128+0.634 filaments are displayed.

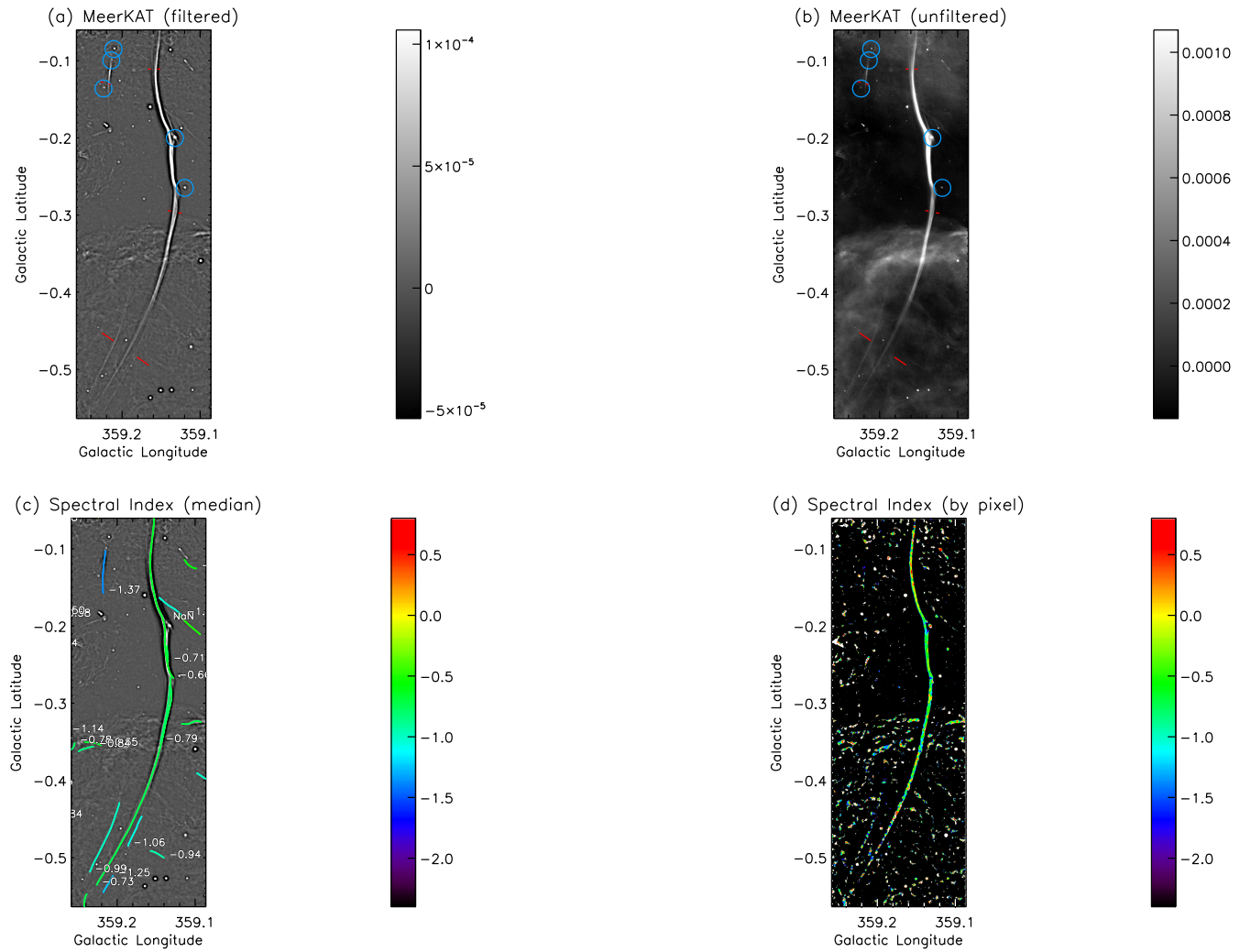


**Figure 5.** (The Snake) Same as Figure 2 except that G359.132-0.296, G359.159-0.111 and G359.196-0.474 filaments are displayed.

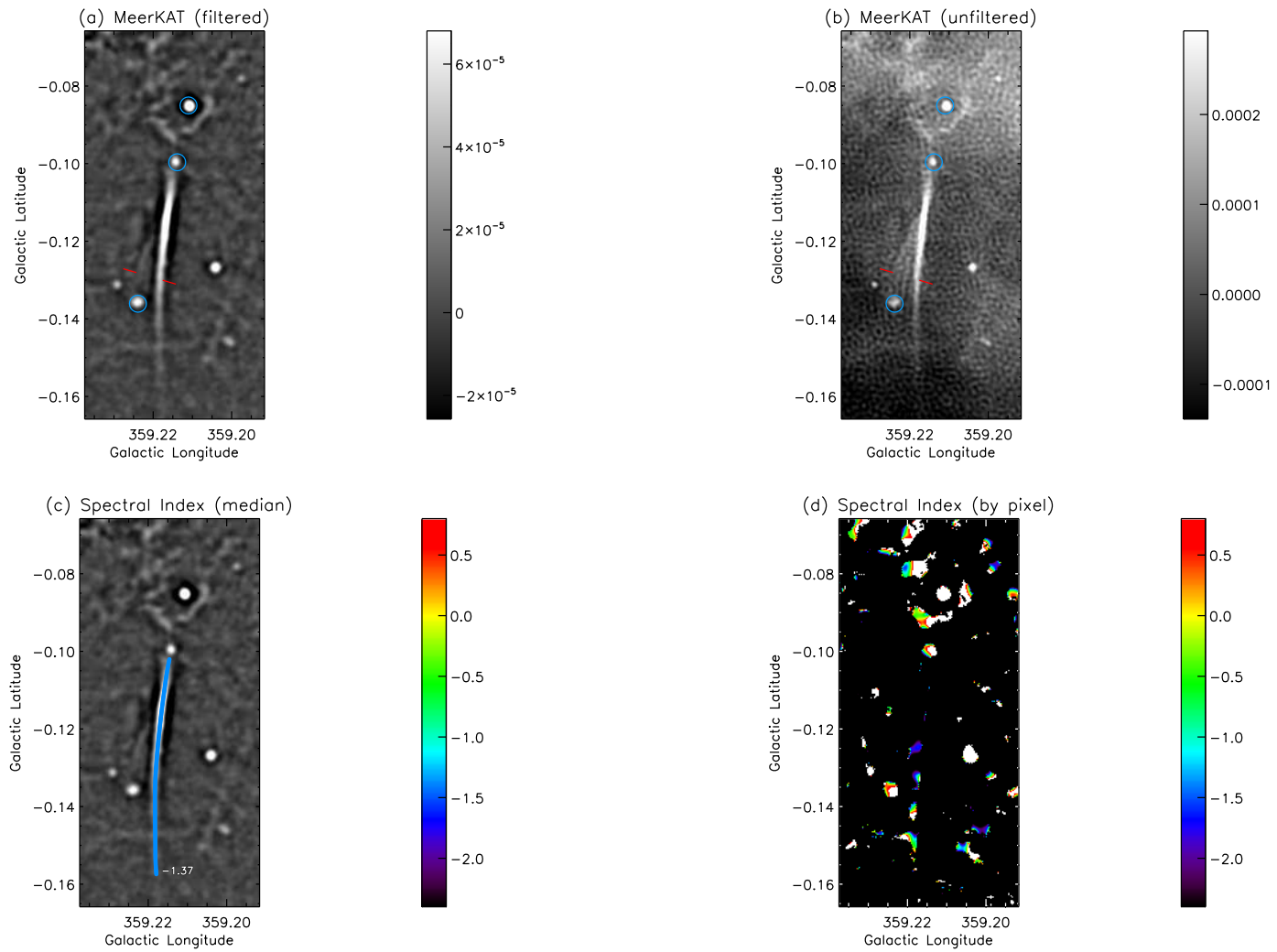


**Figure 6.** (The Candle) Same as Figure 2 except G359.221-0.129 filaments are displayed.

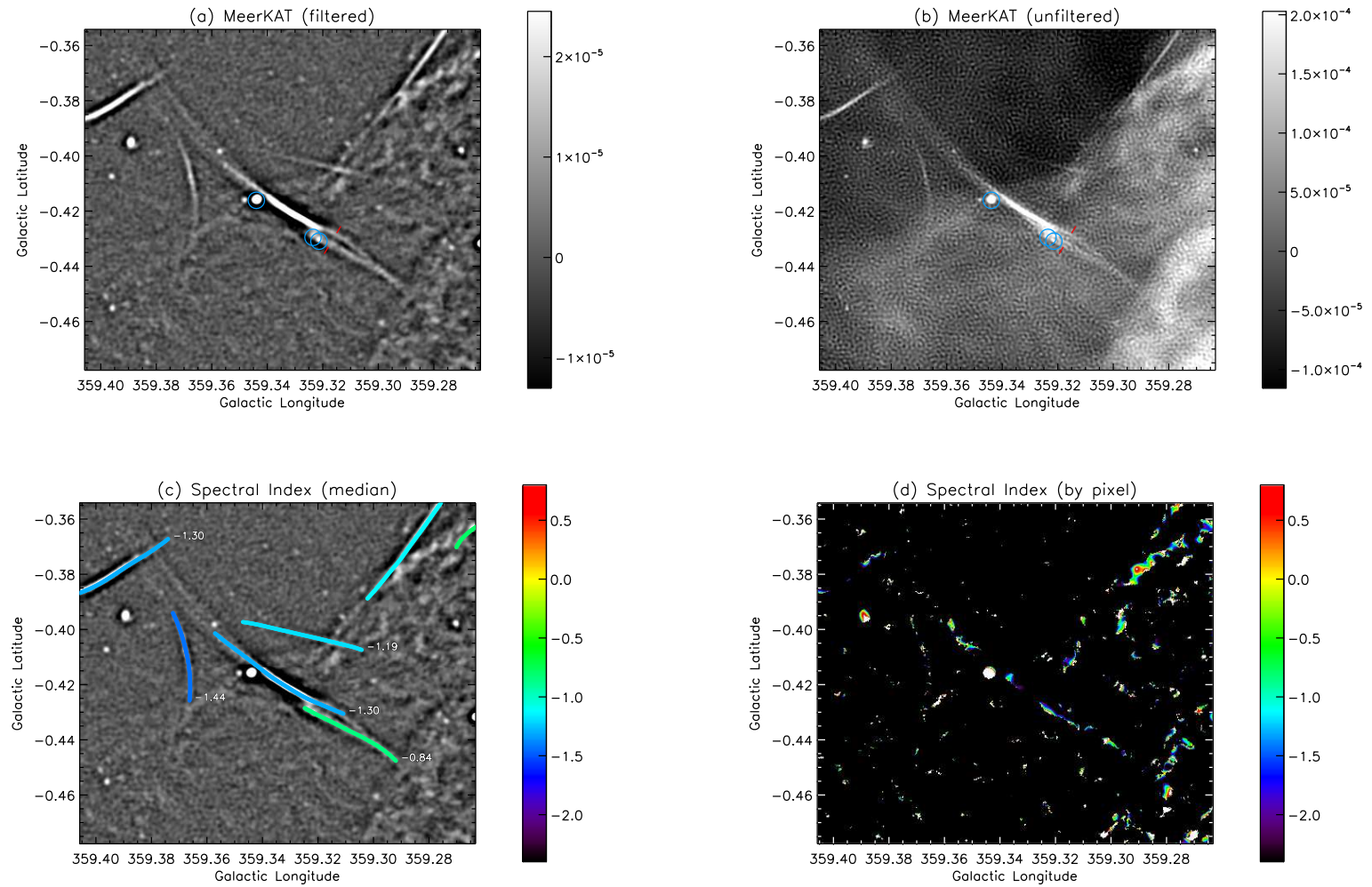


**Figure 7.** (The Sausage) Same as Figure 2 except G359.317-0.430 filaments are displayed.

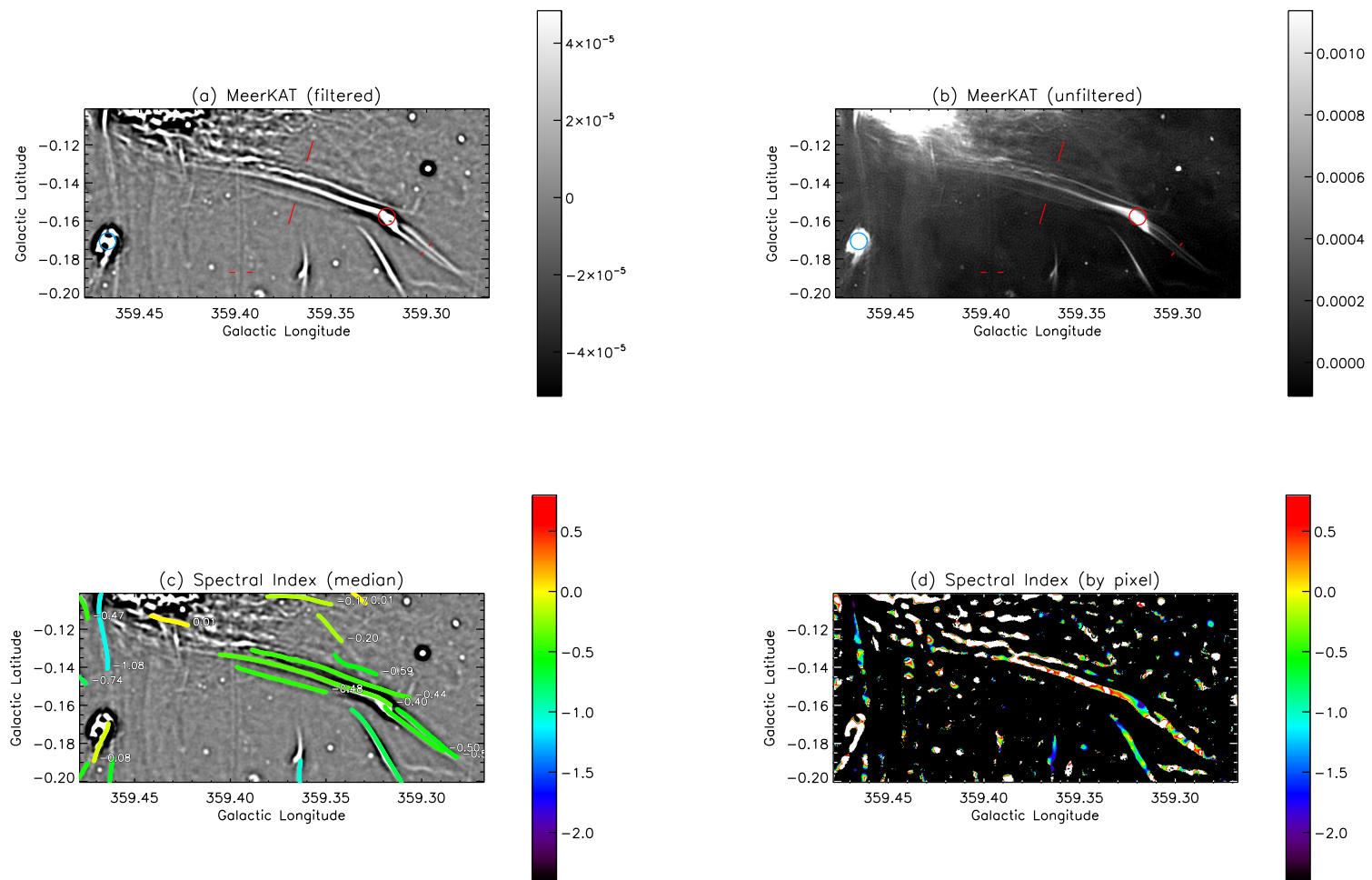


**Figure 8.** (The Hummingbird) Same as Figure 2 except G359.300-0.175, G359.366-0.140, and G359.397-0.187 filaments are displayed.

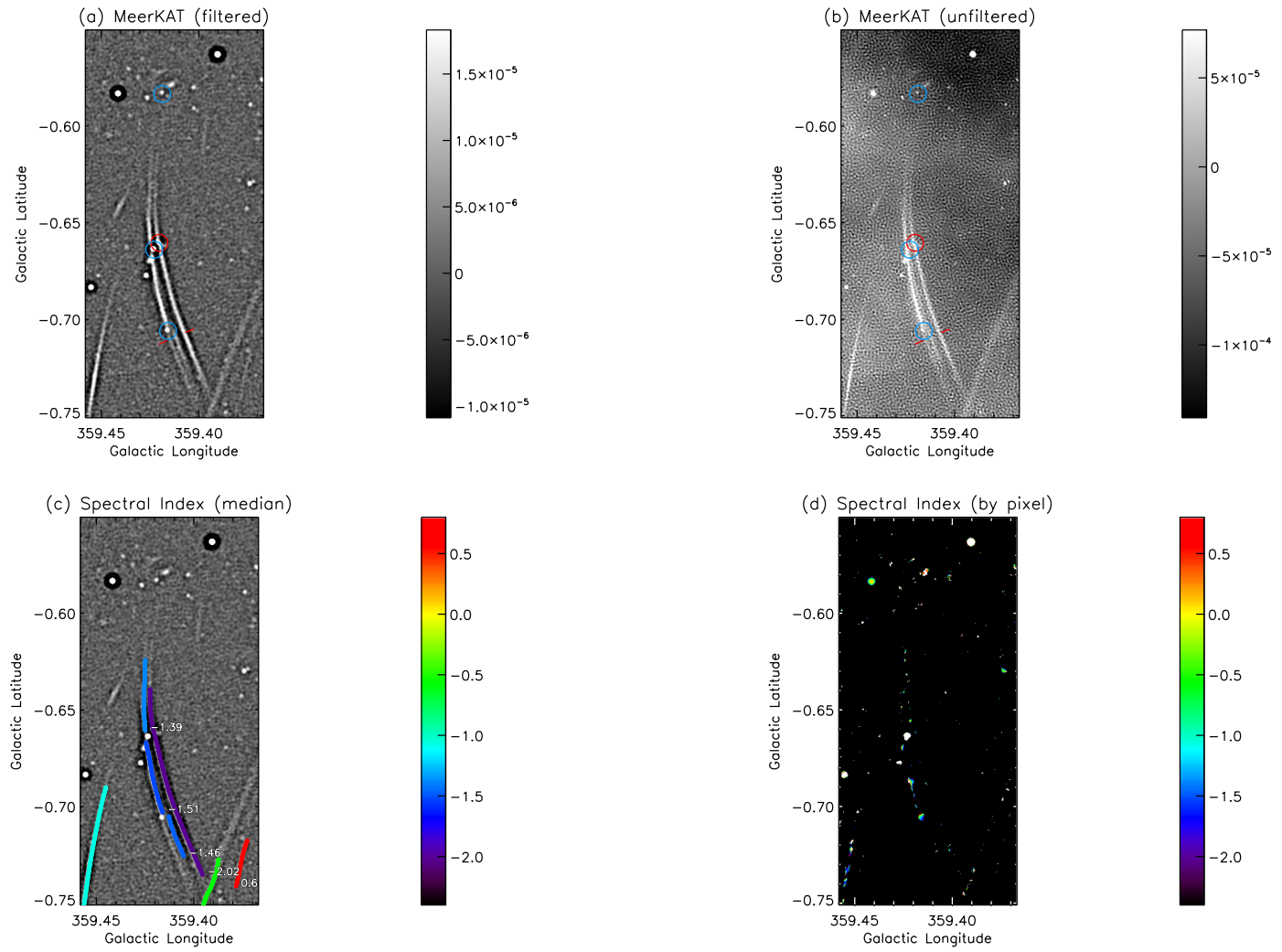


**Figure 9.** (The Feather) Same as Figure 2 except G359.411-0.709 filaments are displayed.

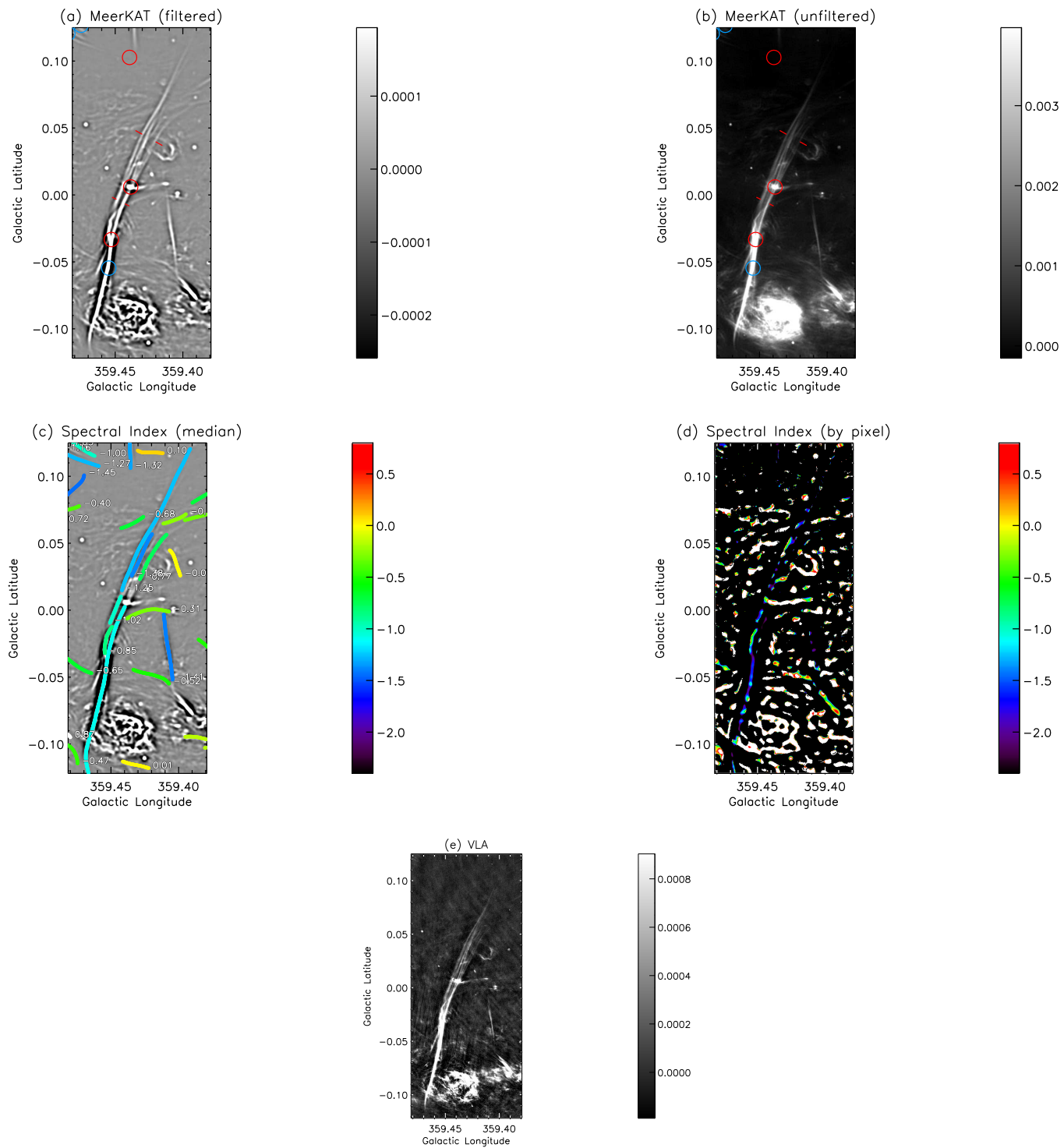


**Figure 10.** (The SgrC) Top four panels are the same as Figure 2 except G359.425+0.043 and G359.446-0.005 filaments displayed. The bottom panel shows a 20cm VLA image of the same region with  $\sim 1''$  spatial resolution.

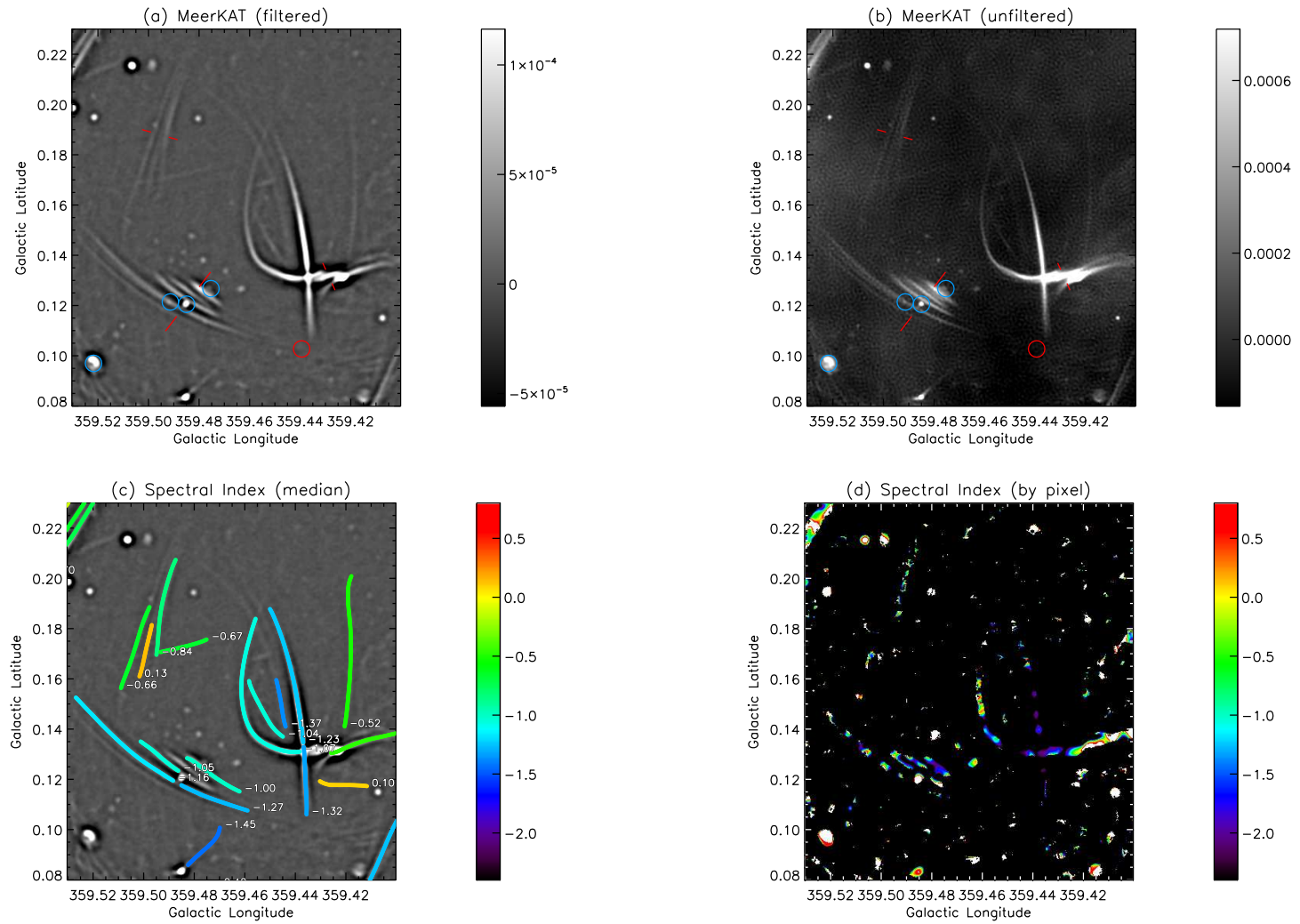


**Figure 11.** (The French Knife and the Concorde) Same as Figure 2 except G359.429+0.132 filaments are displayed

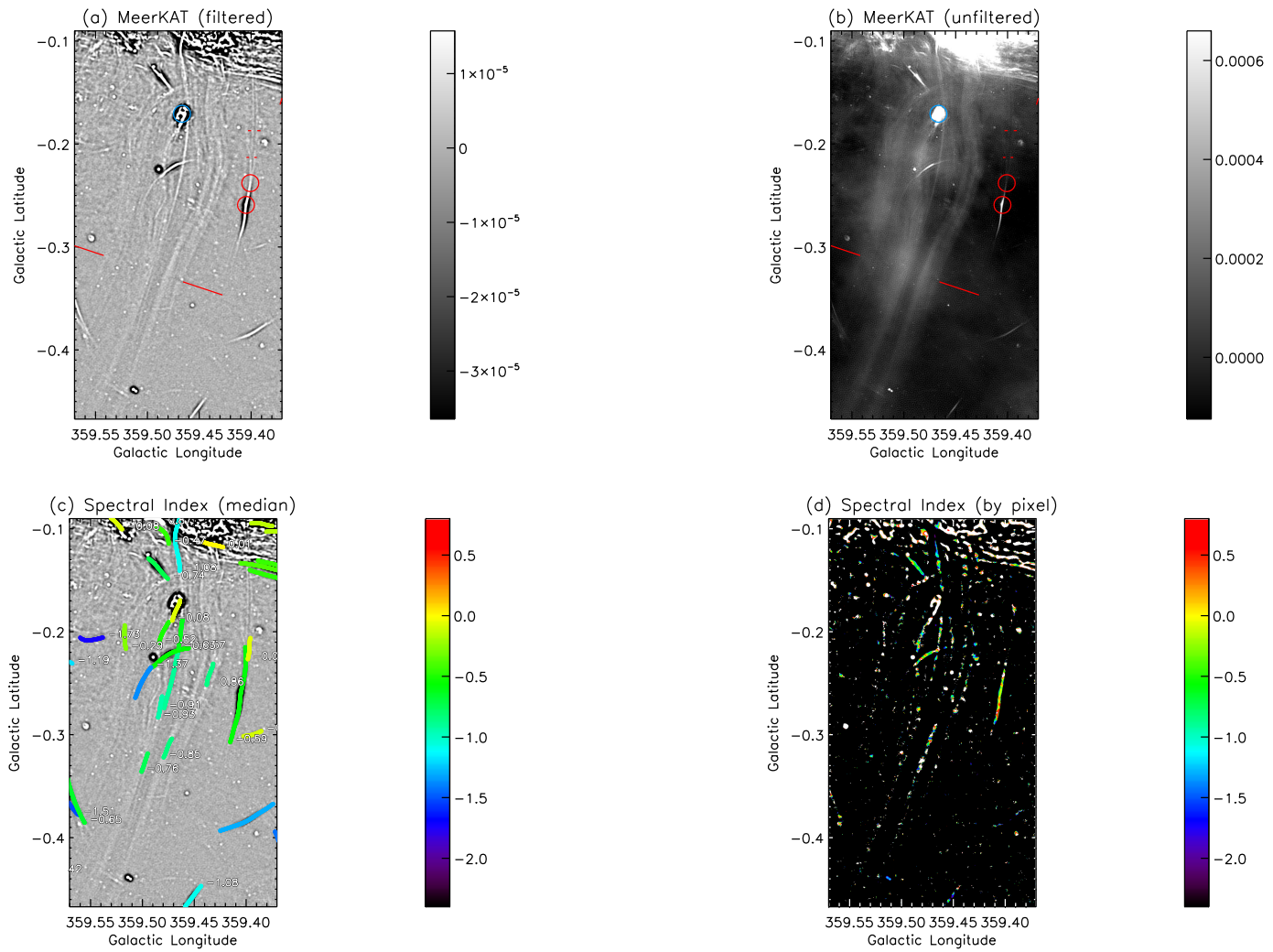


**Figure 12.** (The Cataract, the Forceps and the River) Same as Figure 2 except G359.504-0.321 filaments are displayed.

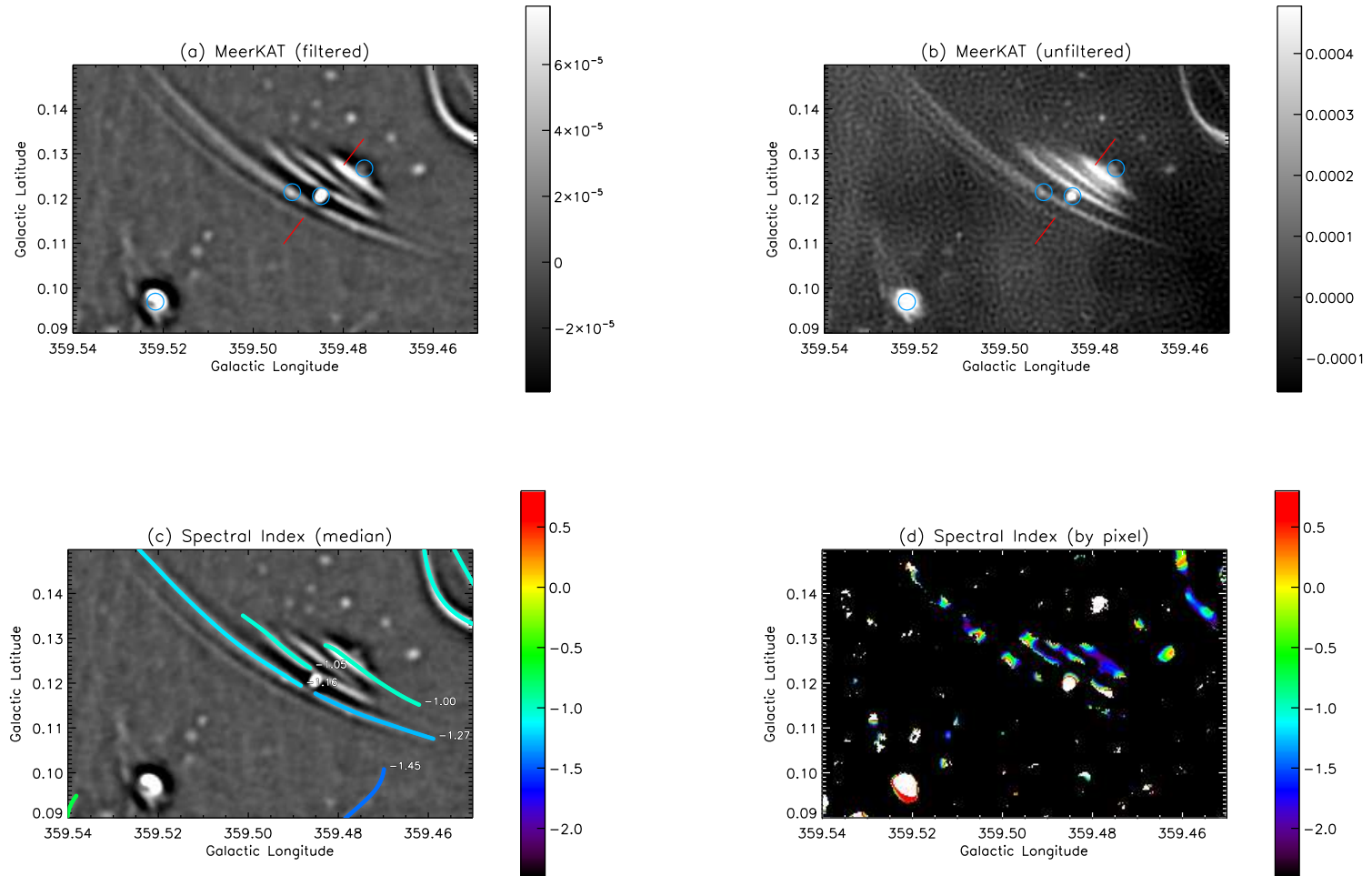


**Figure 13.** (The Bent Harp) Same as Figure 2 except G-0.50+0.12 filaments are displayed

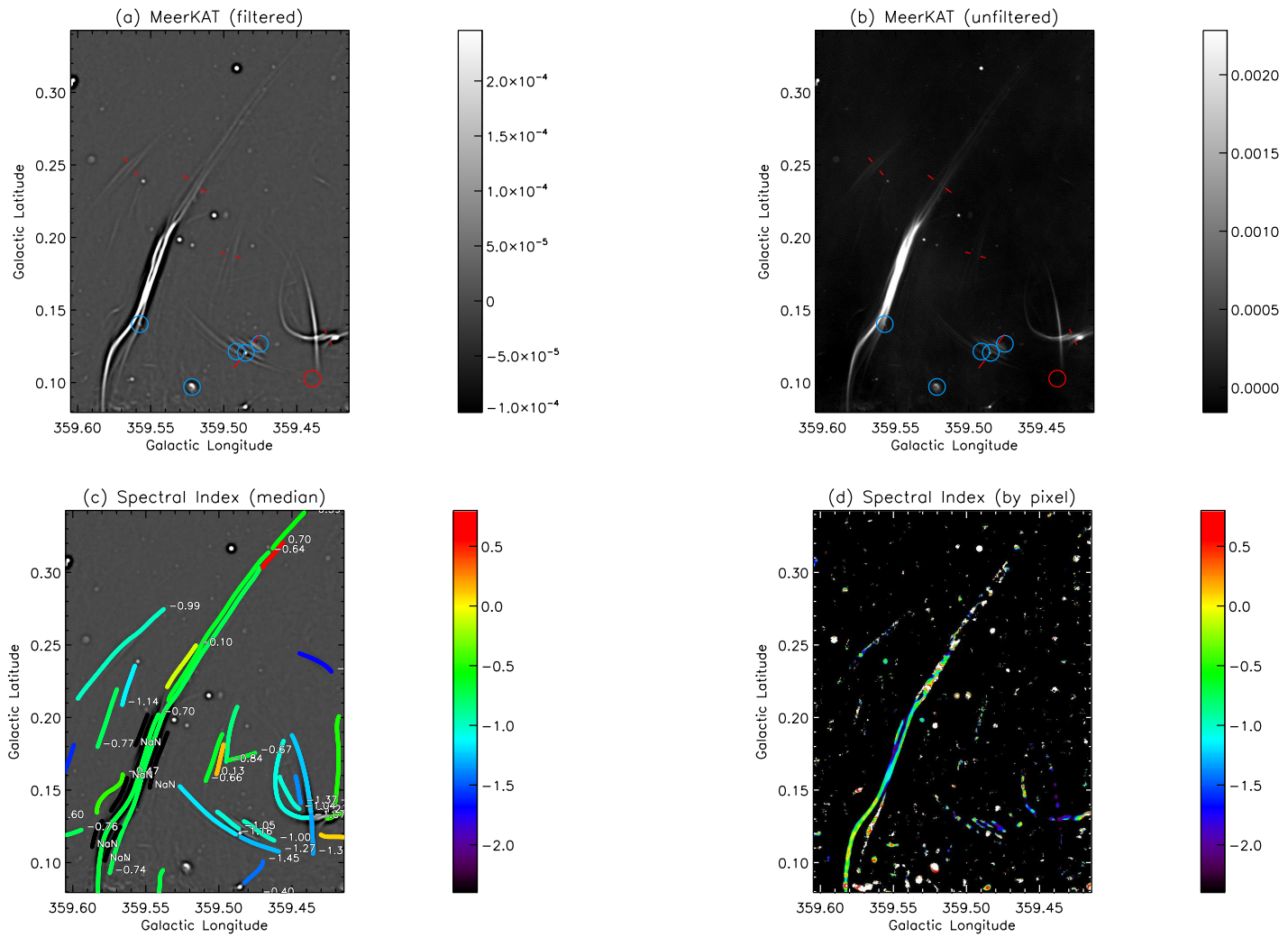


**Figure 14.** (The Ripple and the Edge-on Spiral) Same as Figure 2 except G-0.49+0.21 filaments are displayed.

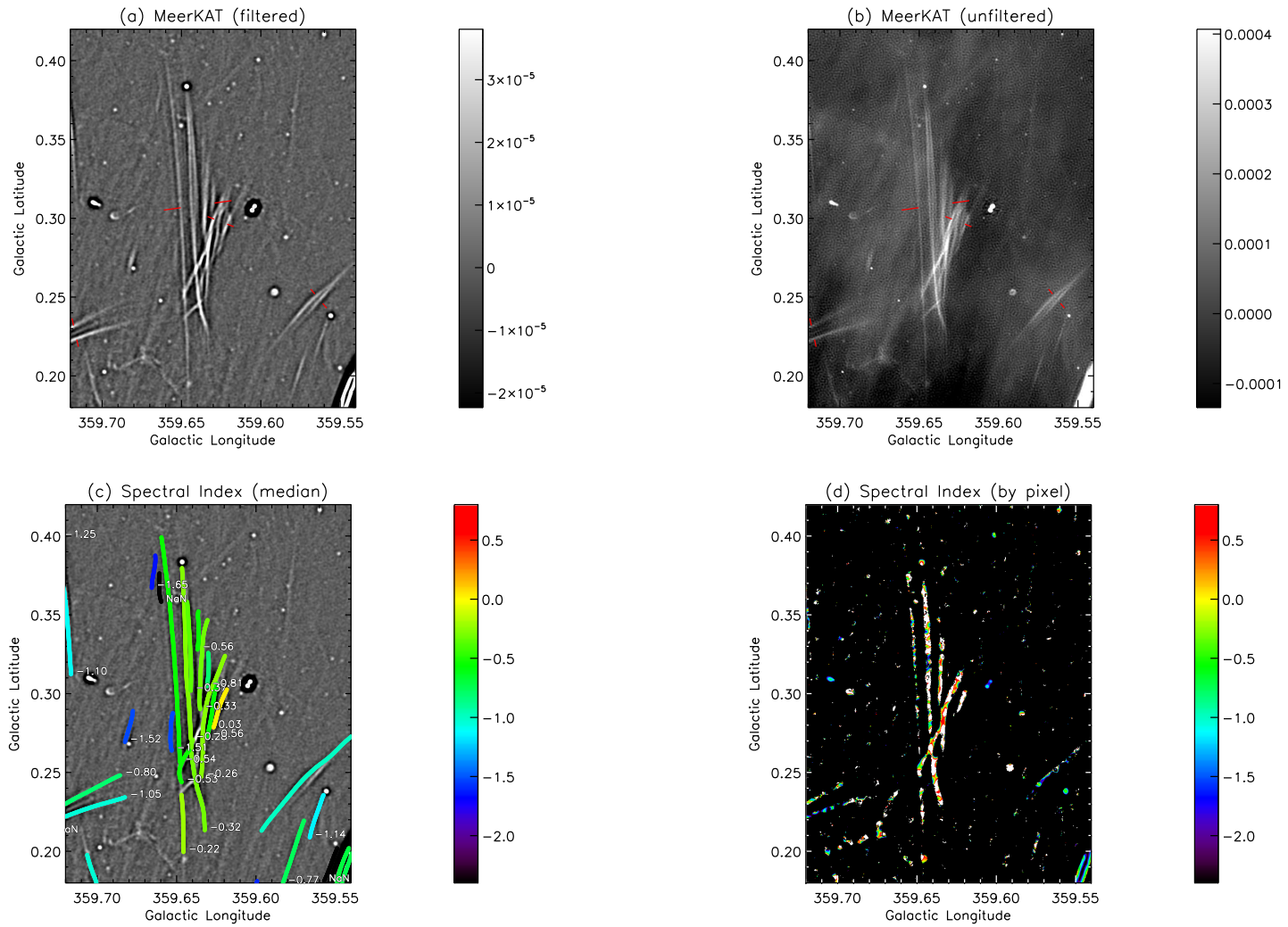


**Figure 15.** (The Broken Harp) Same as Figure 2 except G359.563+0.249, G359.625+0.298 and G359.640+0.308 filaments are displayed.

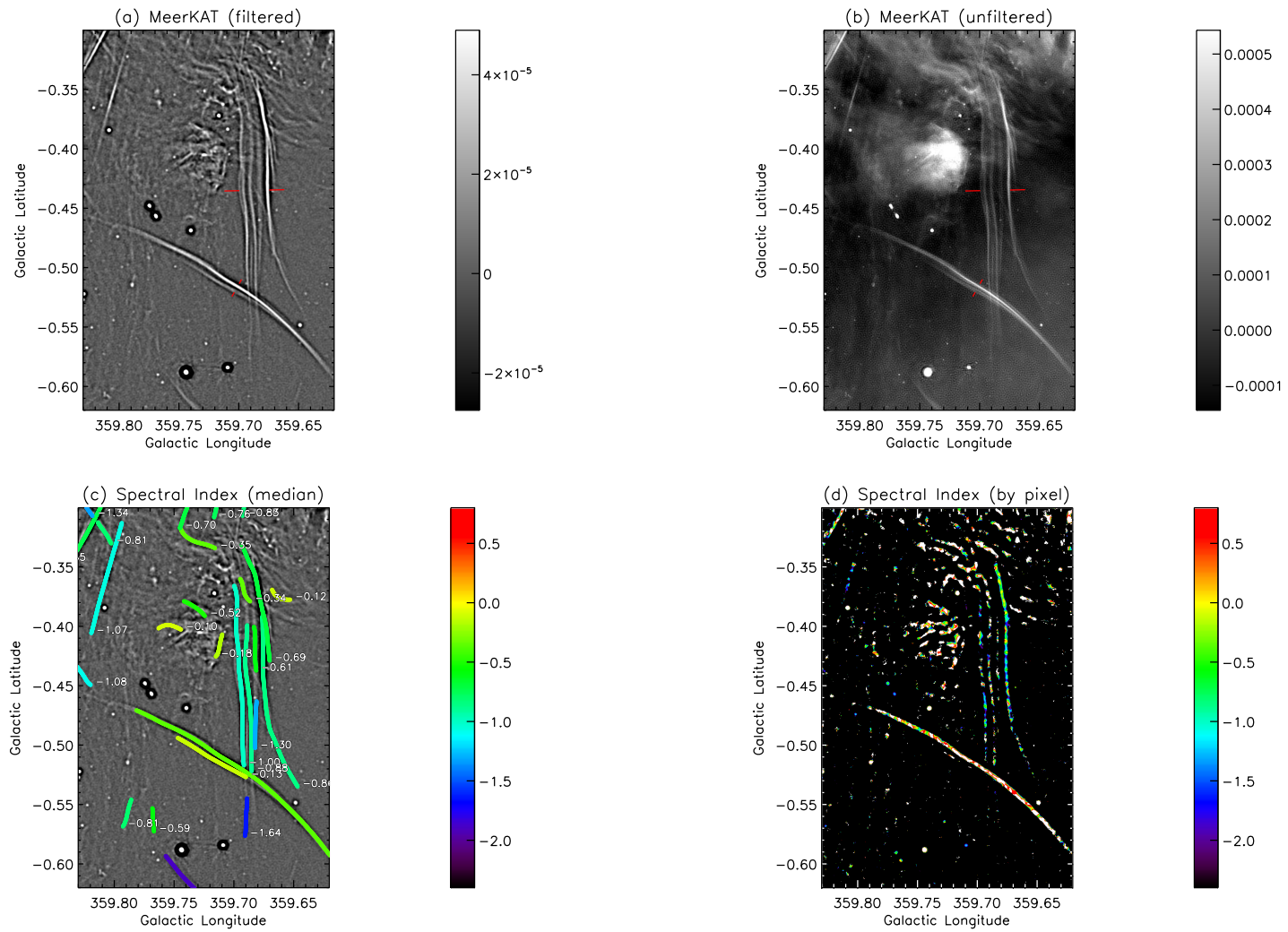


**Figure 16.** (The Waterfall) Same as Figure 2 except G359.687-0.435 and G359.702-0.517 filaments are displayed.

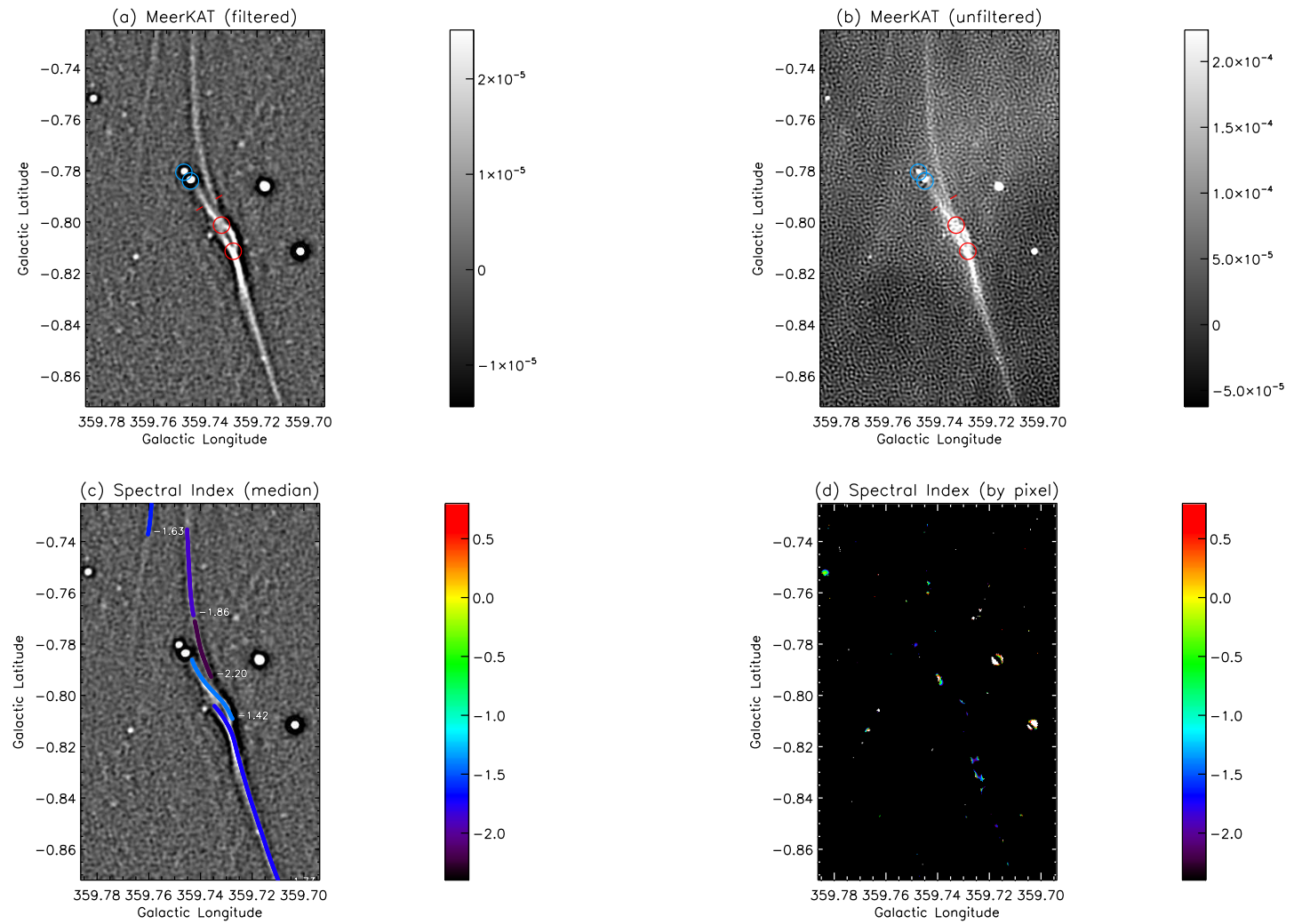


**Figure 17.** (The Knot) Same as Figure 2 except G359.738-0.792 filaments are displayed.

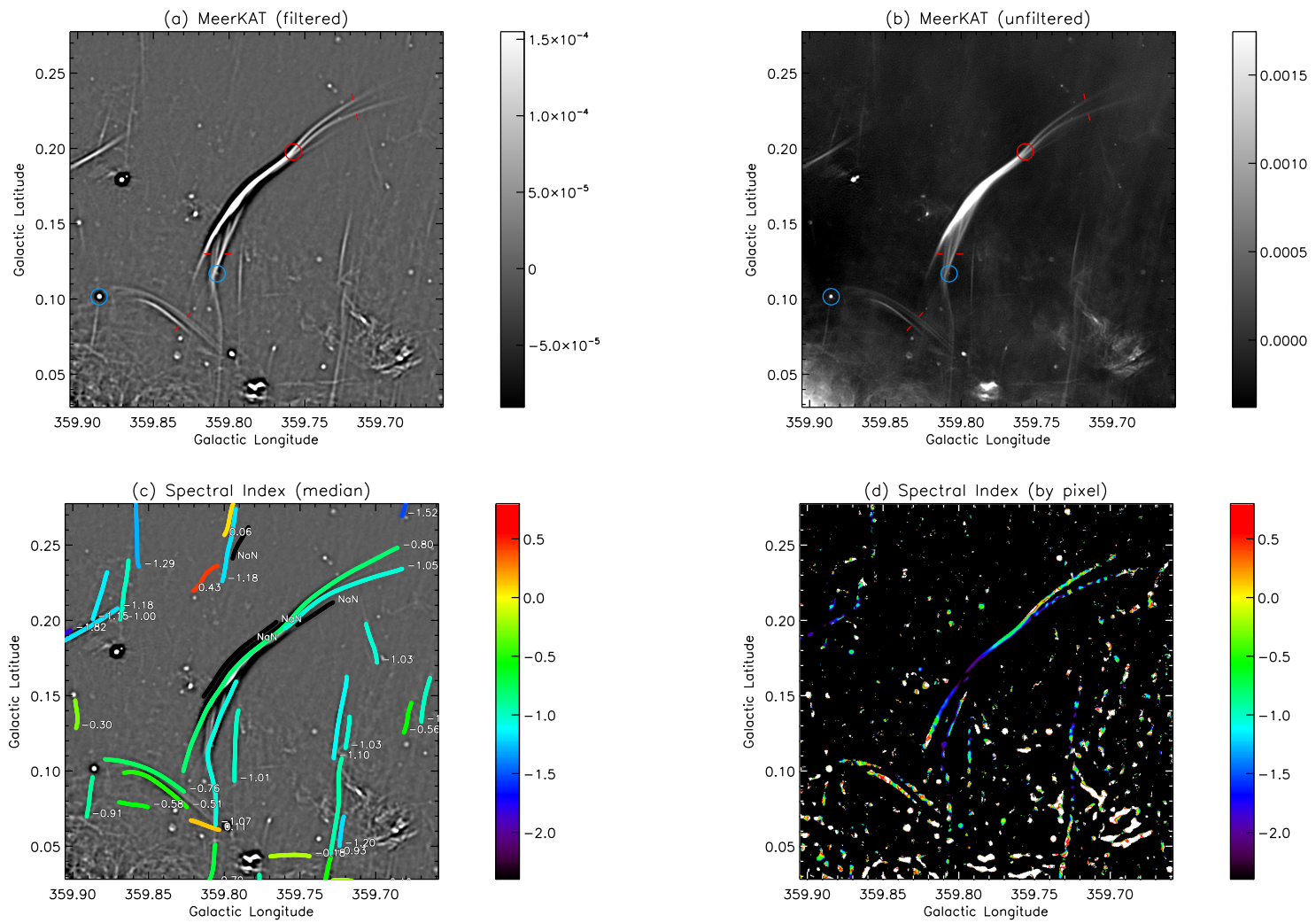


**Figure 18.** (The Flamingo) Same as Figure 2 except G359.808+0.130 and G359.717+0.228 filaments are displayed.

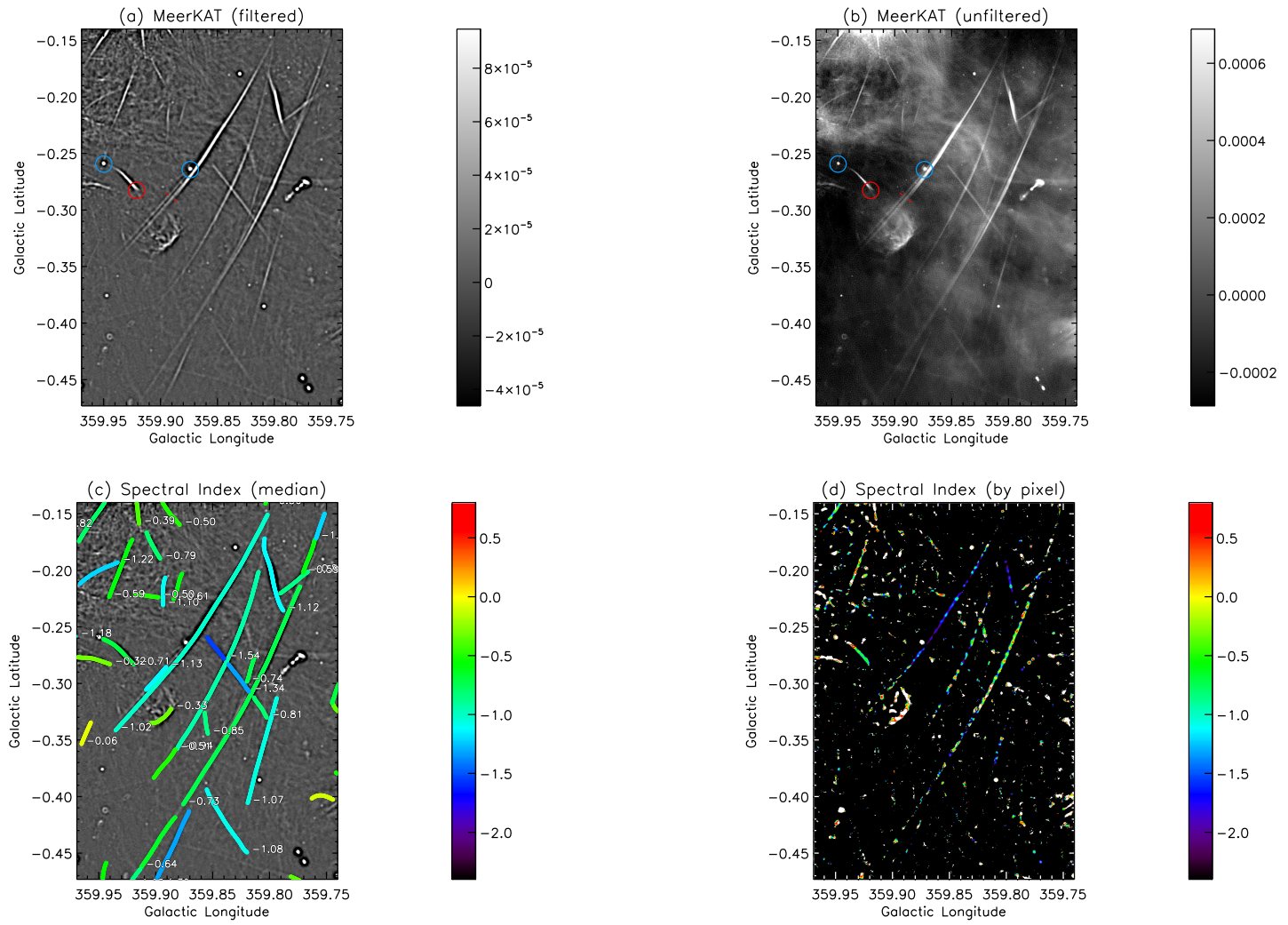


**Figure 19.** (The Cleaver Knife) Same as Figure 2 except G359.890-0.289 filaments are displayed.

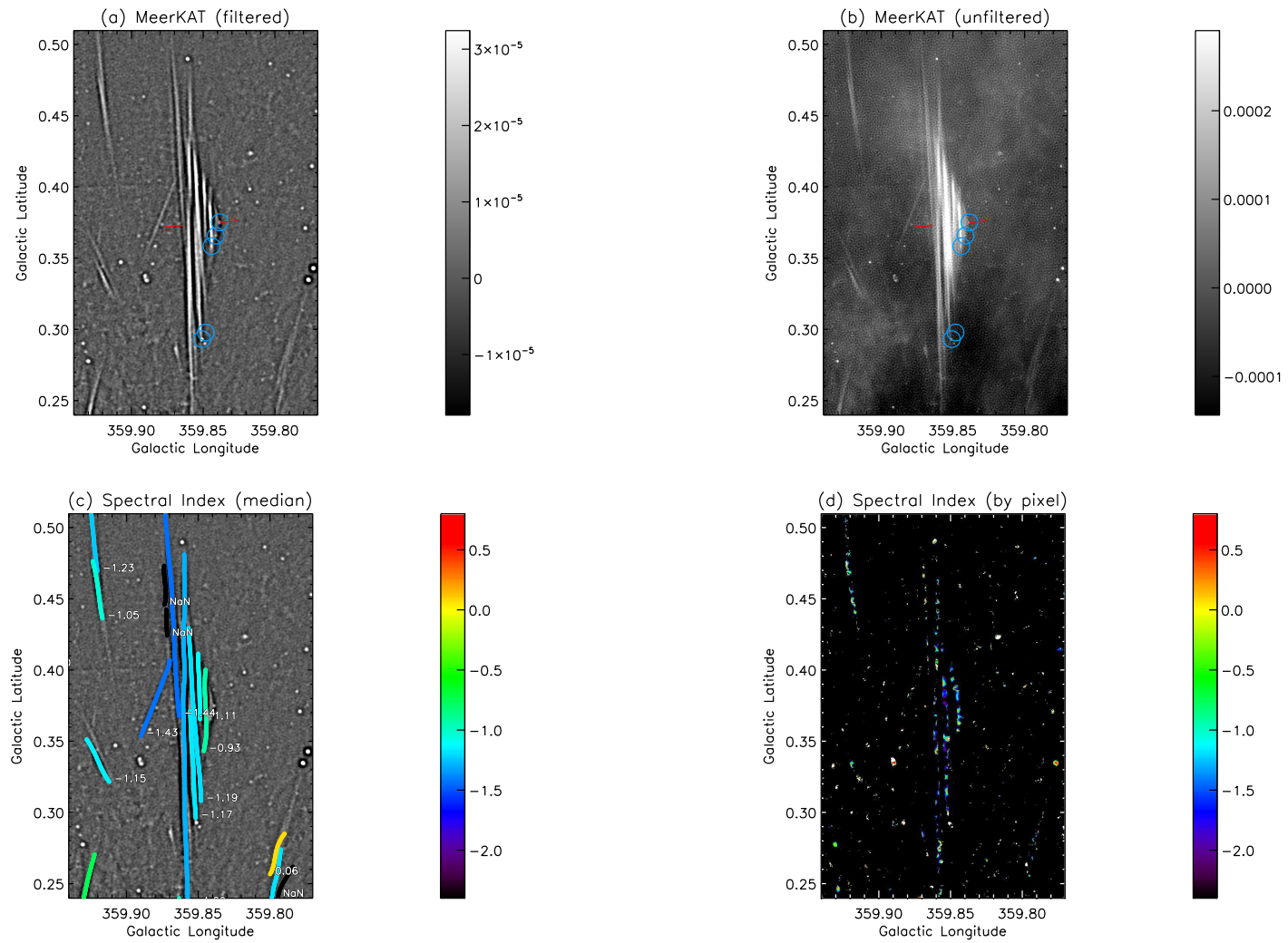


**Figure 20.** (The Harp) Same as Figure 2 except G359.851+0.374 filaments are displayed.

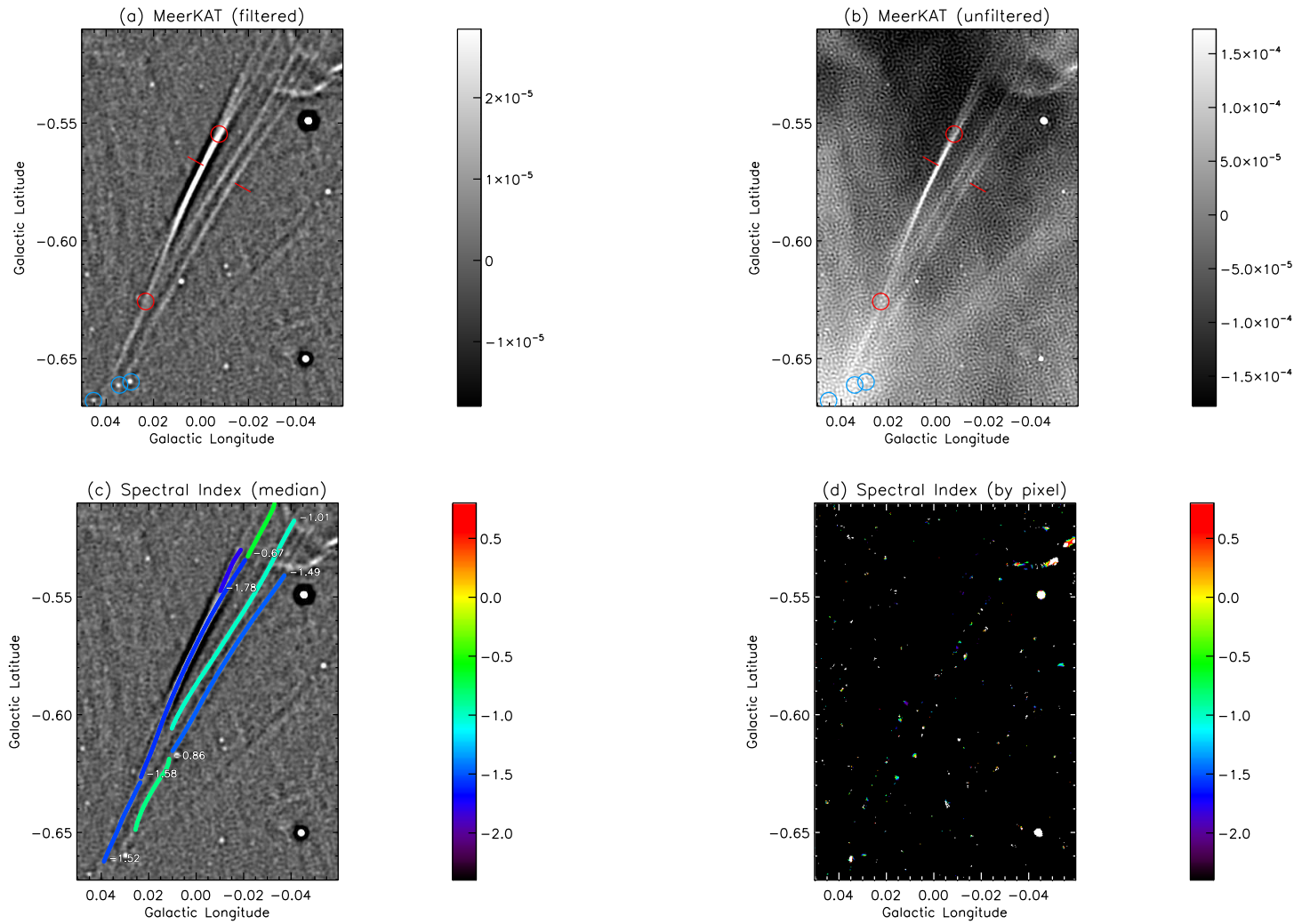


**Figure 21.** (The Comet) Same as Figure 2 except G359.992-0.572 filaments are displayed.

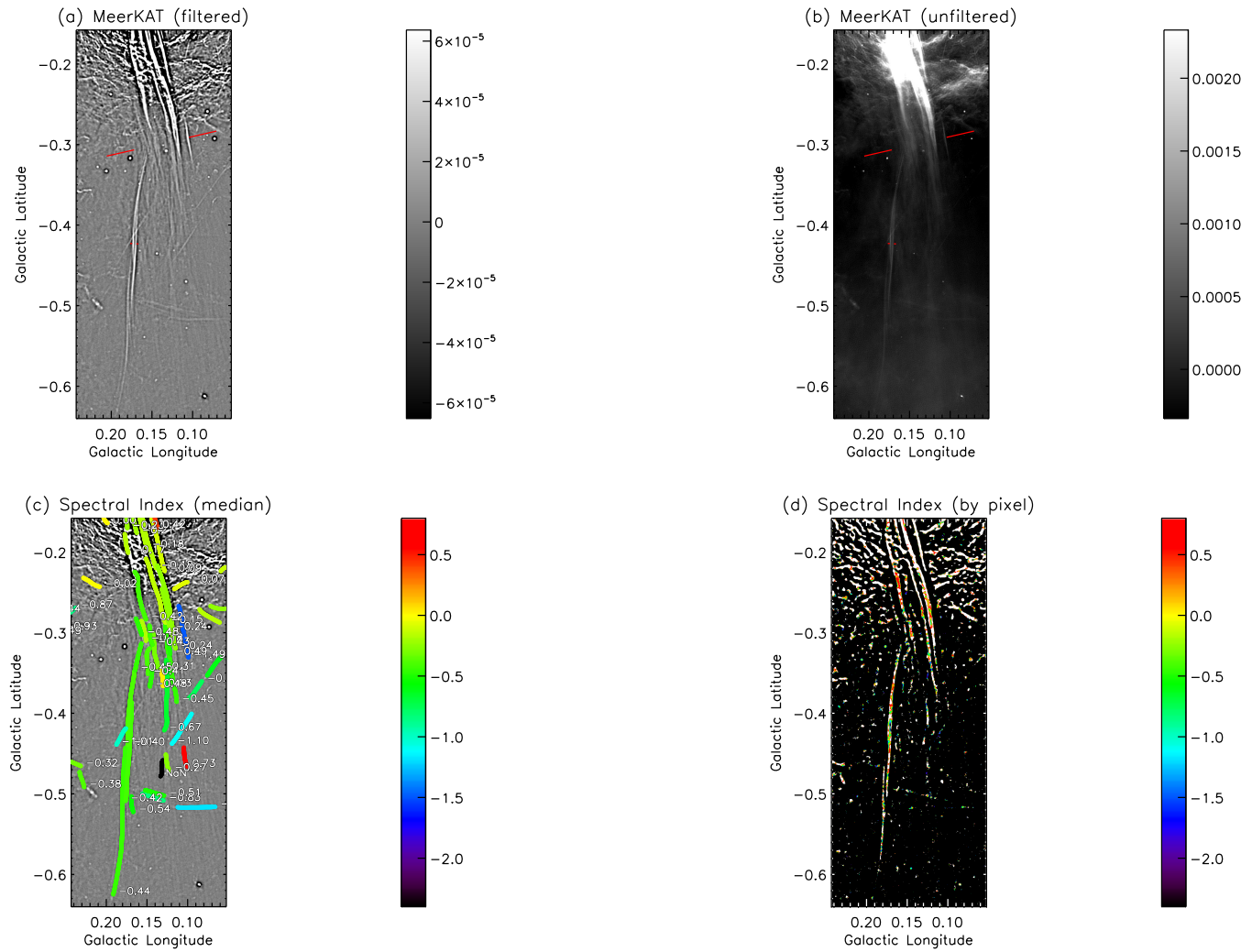


**Figure 22.** (The Radio Arc S) Same as Figure 2 except G0.138-0.299 and G0.172-0.423 filaments are displayed.

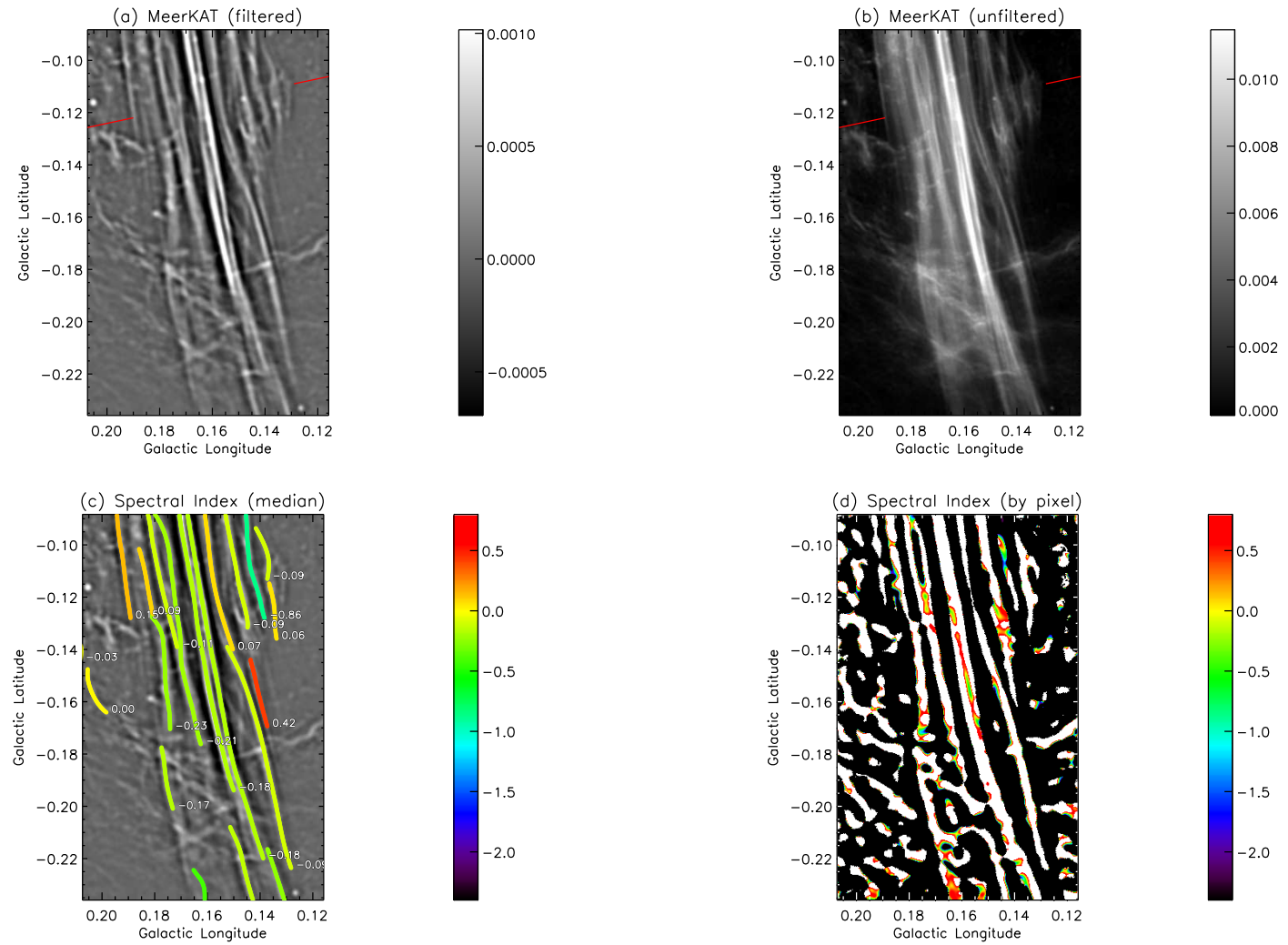


**Figure 23.** (The Radio Arc) Same as Figure 2 except G0.16-0.16 filaments are displayed.



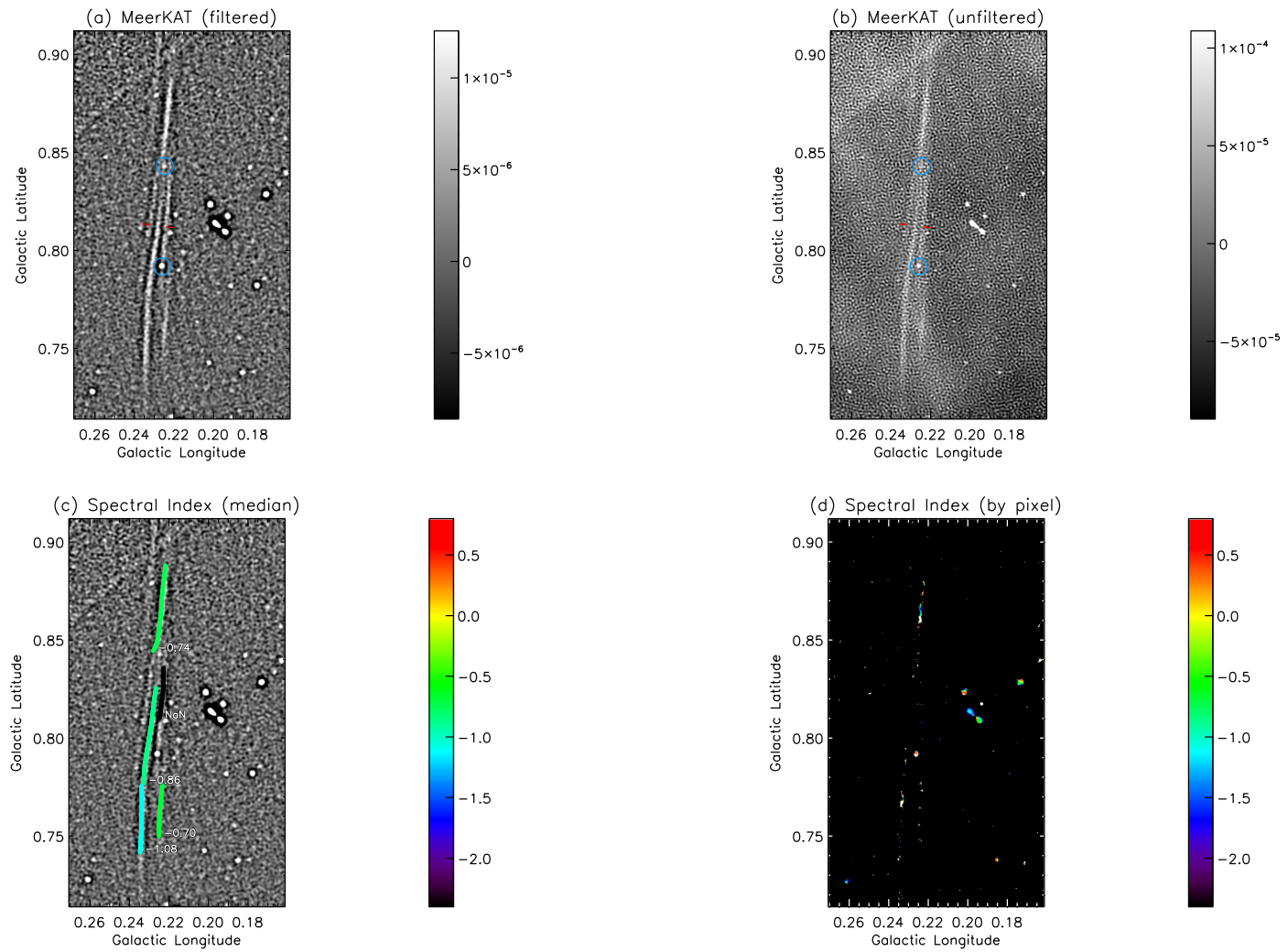


**Figure 25.** (The Space Shuttle) Same as Figure 2 except G0.22+0.81 filaments are displayed.

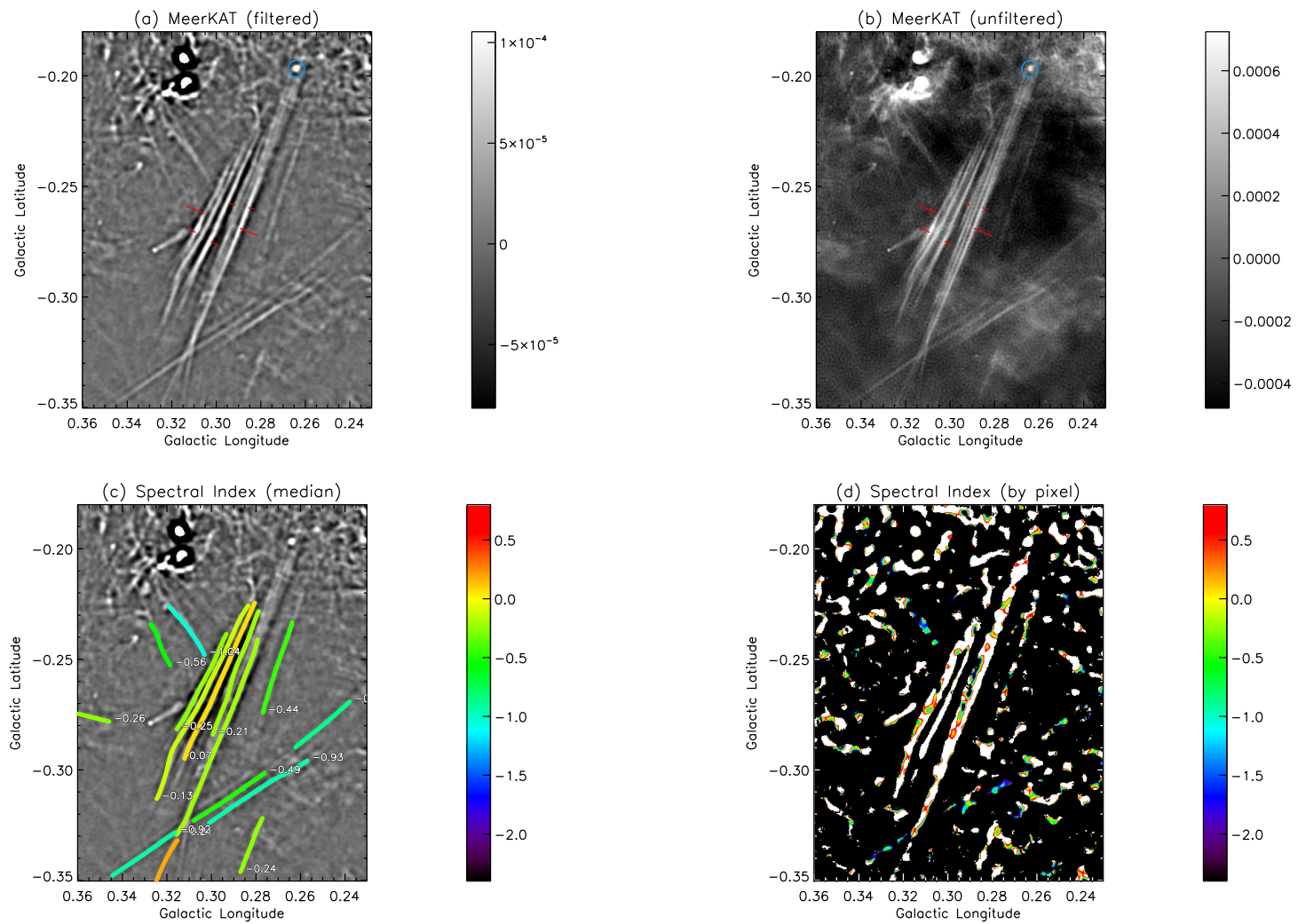


**Figure 26.** (The Porcupine) Same as Figure 2 except G0.30-0.26 filaments are displayed.

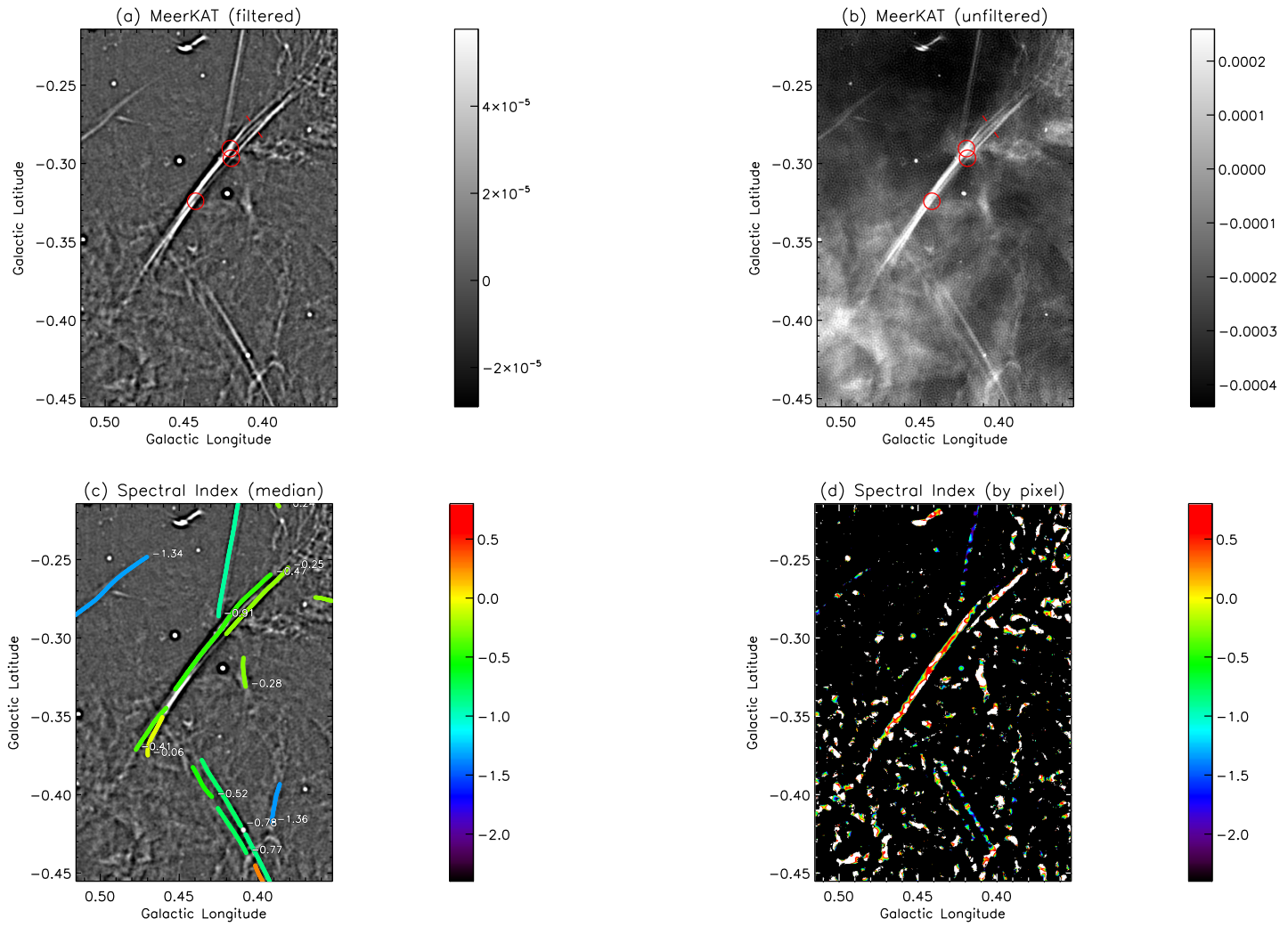


**Figure 27.** (The Contrail) Same as Figure 2 except G0.43-0.33 filaments are displayed.

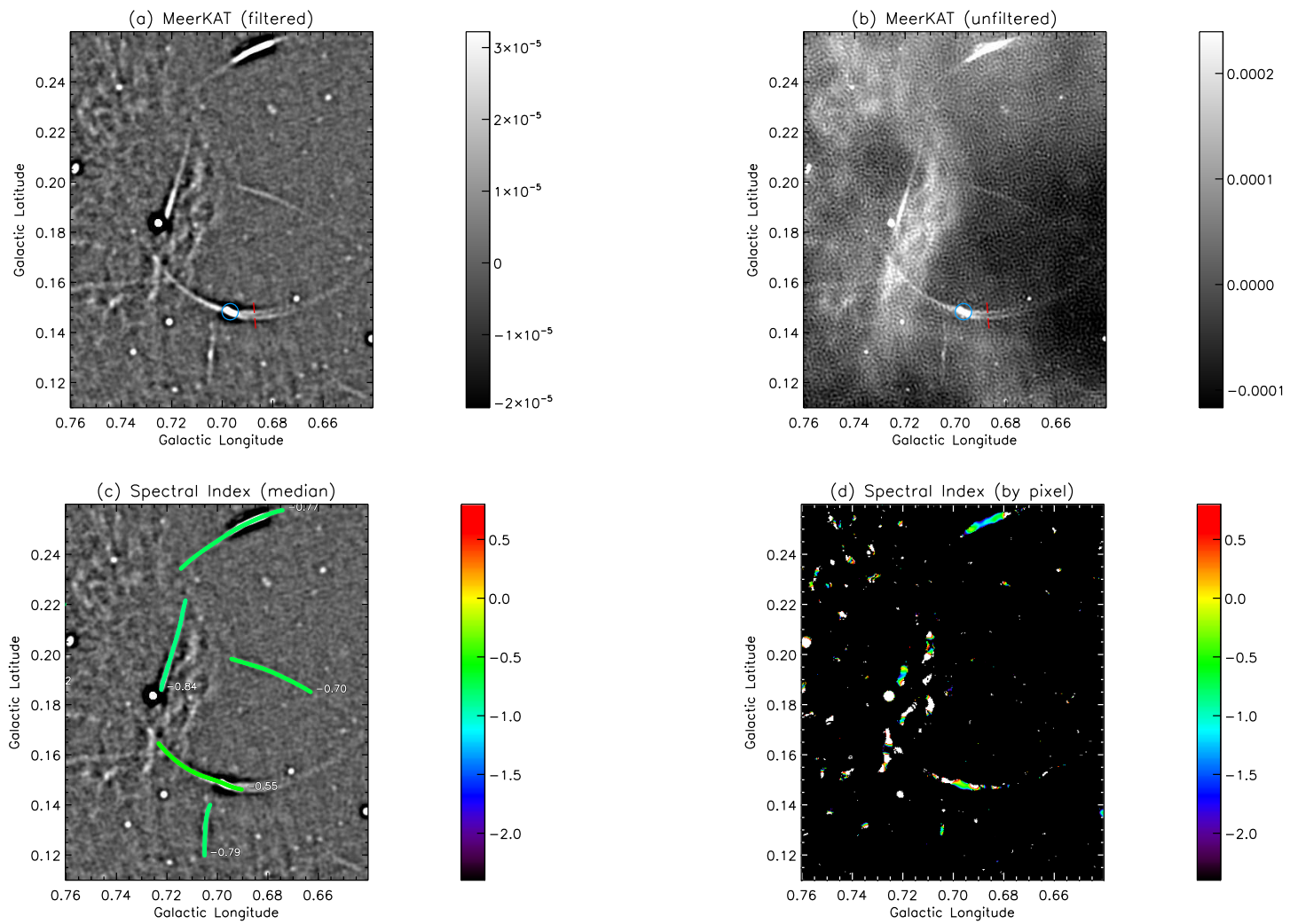


**Figure 28.** (The Bent Fork) Same as Figure 2 except G0.70+0.19 filaments are displayed.

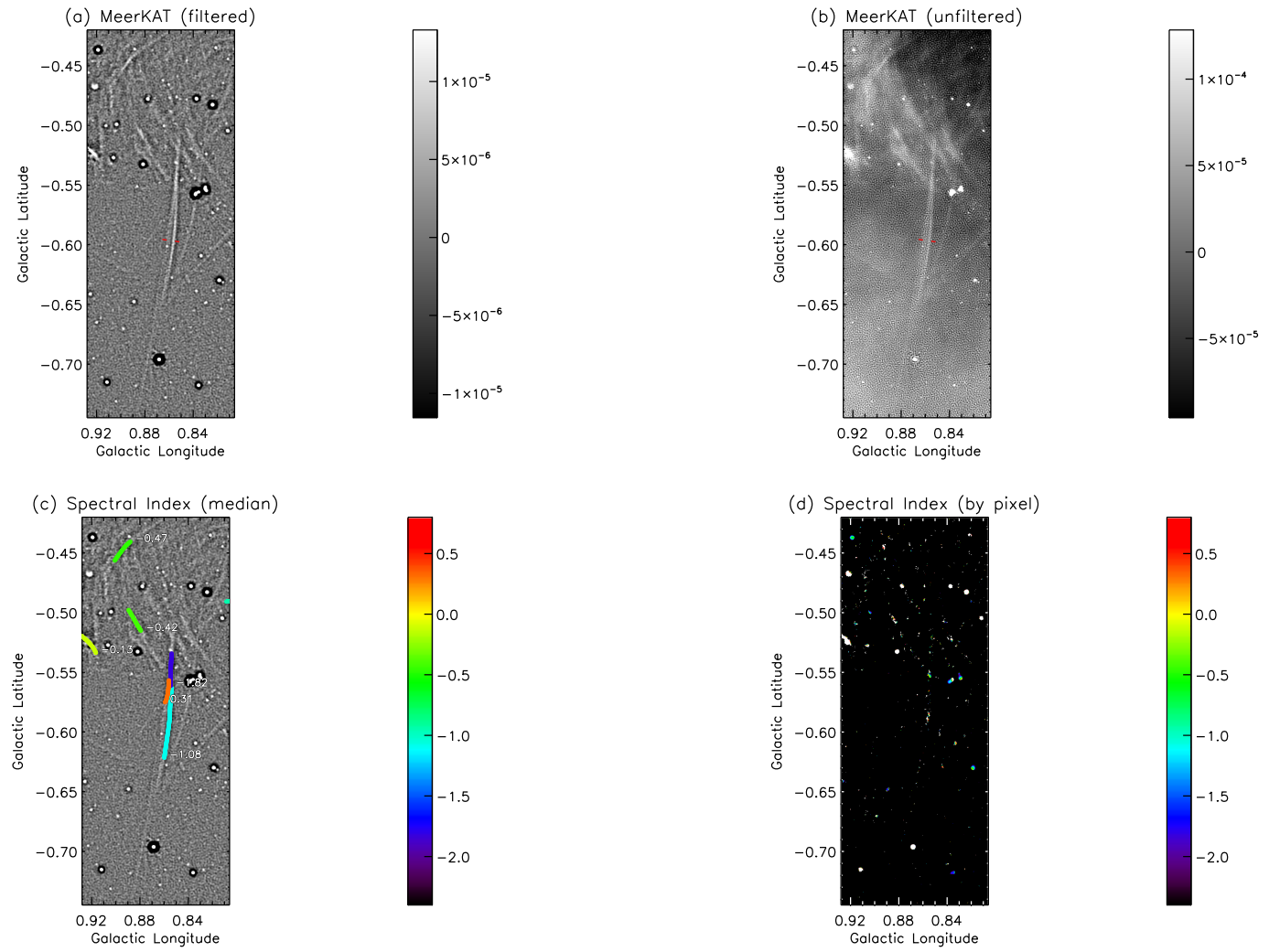


**Figure 29.** (The Meteor) Same as Figure 2 except G0.87-0.58 filaments are displayed.

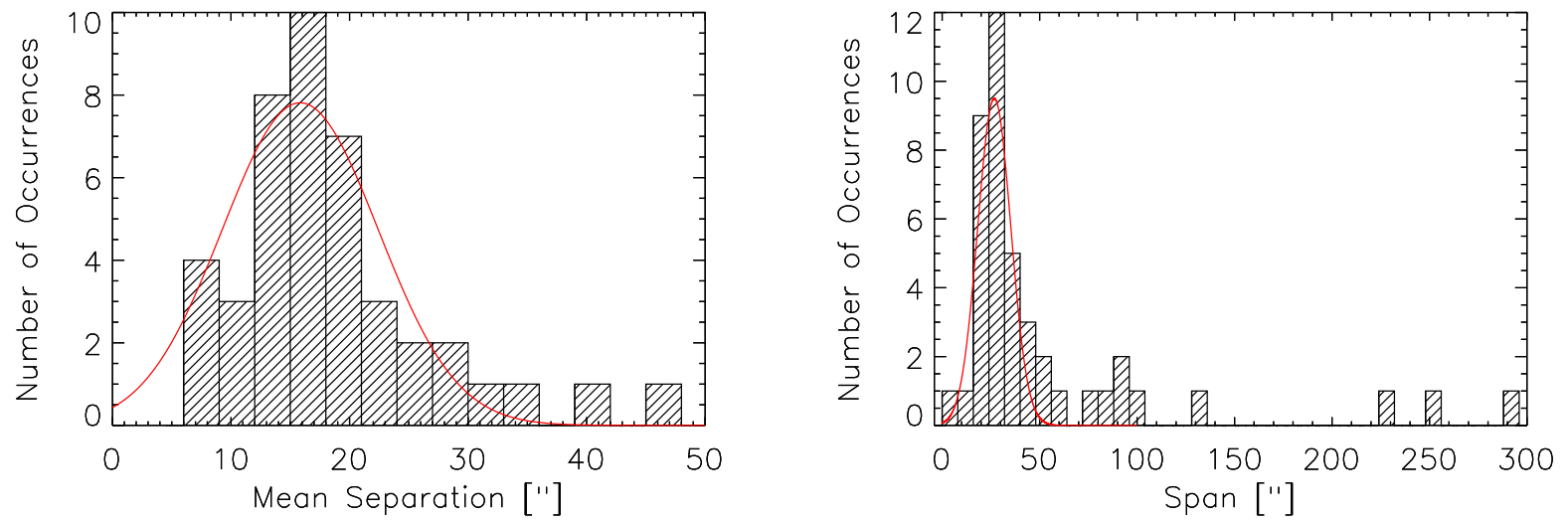


**Figure 30.** Histograms of the mean separation of filaments (left) and the total span or width (right) for the 42 cross sections listed in Table 1 and indicated in the previous figures. Gaussian fits to characterize the distributions are shown as red lines. Parameters of the Gaussian fits are listed at the bottom of Table 1.

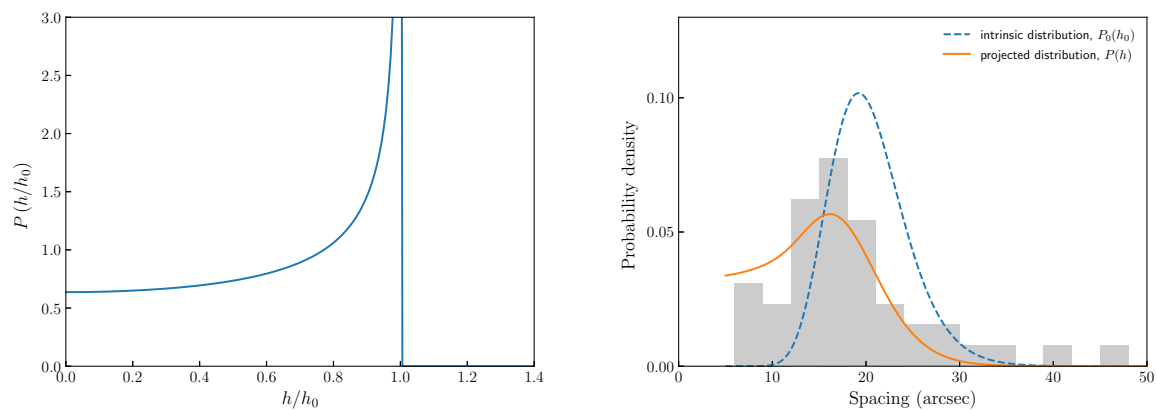


**Figure 31.** Distribution of apparent filament spacings (ie. as observed on the sky) for a filament population with fixed true spacing  $h_0$ . Comparison of a lognormal intrinsic filament spacing distribution (blue dashed curve), the resulting distribution of spacings on the sky (orange curve) and the observed distribution.

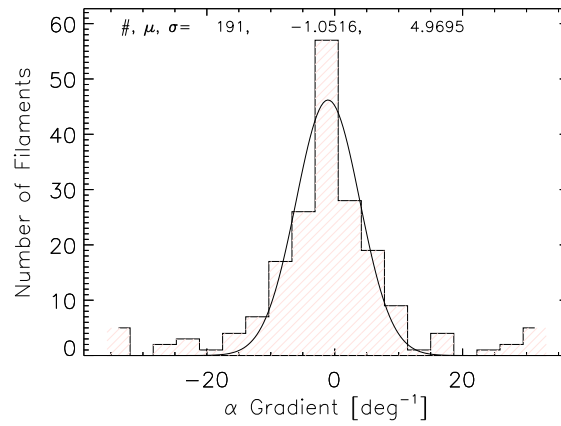


**Figure 32.** A histogram of the linear gradients in spectral index,  $\alpha$ , as a function of position along the filament for 191 long filaments in the Galactic center. The distribution is characterized by a Gaussian function with a mean ( $\mu$ ) of  $-1.1 \text{ deg}^{-1}$  and a dispersion ( $\sigma$ ) of  $5 \text{ deg}^{-1}$ . The negative value of the mean gradient indicates an overall tendency for filaments to steepen with distance from the Galactic plane. The weights are uniform for intensities  $I > 10^{-4} \text{ Jy beam}^{-1}$ , and are taken to be proportional to  $I^2$  at fainter levels. Gradients are estimated using weighted linear fits between  $s$  and  $\alpha$ . The negative value of the mean gradient indicates an overall tendency for filaments to steepen with distance from the Galactic plane, although exceptions to this trend are abundant.